

**APPLICATION OF THE RUZE EQUATION FOR INFLATABLE  
APERTURE ANTENNAS**

BRYAN WELCH

Bachelor of Science in Electrical Engineering

Cleveland State University

May, 2003

submitted in partial fulfillment of requirements for the degree

**MASTER OF SCIENCE IN ELECTRICAL ENGINEERING**

at the

**CLEVELAND STATE UNIVERSITY**

December, 2006

This thesis has been approved  
for the Department of Electrical and Computer Engineering  
and the College of Graduate Studies by

---

Thesis Committee Chairperson, Fuqin Xiong

---

Department/Date

---

Thesis Advisor, Murad Hizlan

---

Department/Date

---

Zhiqiang Gao

---

Department/Date

---

Ana Stankovic

---

Department/Date

---

Robert Romanofsky

---

Department/Date

## **ACKNOWLEDGEMENTS**

Many thanks to my mentor and colleague, Dr. Robert Romanofsky, for encouraging me to perform this study. Thank you to Dr. Murad Hizlan for support and clarity along my pursuit of my Master's Degree. Thank you to NASA Glenn Research Center for providing me the opportunity to pursue my Master's Degree. Finally, I would like to say thank you to my wife Samantha, for all of her editorial assistance and for always standing beside me with encouragement along the way.

# **APPLICATION OF THE RUZE EQUATION FOR INFLATABLE APERTURE ANTENNAS**

BRYAN WELCH

## **ABSTRACT**

Inflatable aperture reflector antennas are an emerging technology that NASA is investigating for potential uses in science and exploration missions. As inflatable aperture antennas have not been proven fully qualified for space missions, they must be characterized properly so that the behavior of the antennas can be known in advance. In order to properly characterize the inflatable aperture antenna, testing must be performed in a relevant environment such as a vacuum chamber. Since the capability of having a Radio Frequency (RF) test facility inside a vacuum chamber does not exist at NASA Glenn Research Center, a different technique must be utilized.

The proposed idea to test an inflatable aperture antenna in a vacuum chamber would be to perform a photogrammetry study of the inflatable aperture antenna surface using laser ranging measurements. A Root Mean Square (RMS) error term would be derived from the photogrammetry study to calculate the antenna surface loss as described by the Ruze Equation. However, initial testing has shown that problems exist with using the Ruze Equation to calculate the loss due to errors in the antenna surface.

This study utilizes RF measurements obtained in a Near-Field antenna range and photogrammetry data taken from a laser range scanner to compare the expected performance of the test antenna, via the Ruze Equation, with the actual RF patterns and directivity measurements. Results show that the Ruze Equation overstates the degradation in the directivity calculation. Therefore, when the photogrammetry study is performed on the test antennas in the vacuum chamber, a more complex equation must be used, due to the fact that the Ruze theory overstates the loss in directivity for inflatable aperture reflector antennas.

# TABLE OF CONTENTS

	<b>Page</b>
<b>LIST OF TABLES .....</b>	<b>VIII</b>
<b>LIST OF FIGURES .....</b>	<b>IX</b>
<b>I INTRODUCTION .....</b>	<b>1</b>
1.1 Intended Purpose of Work .....	2
1.2 Background Introduction .....	4
1.3 Chapter Topics .....	5
<b>II BACKGROUND INFORMATION .....</b>	<b>7</b>
2.1 Inflatable Aperture Antennas .....	7
2.2 Ruze Theory .....	12
2.3 RMS Error Calculation .....	23
2.4 Antenna Surface Sampling Requirements .....	25
<b>III EQUIPMENT AND METHODOLOGY .....</b>	<b>28</b>
3.1 Offset Inflatable Aperture Antenna Specifications .....	28
3.2 Planar Near-Field Antenna Test Facility .....	31
3.3 Leica 200 Photogrammetry System .....	34
3.4 Data Transformation Routine .....	36
<b>IV RESULTS .....</b>	<b>38</b>

4.1	RF Performance .....	38
4.2	RMS Performance .....	51
4.3	Ruze Equation Performance .....	70
<b>V</b>	<b>CONCLUSIONS .....</b>	<b>72</b>
<b>VI</b>	<b>FUTURE WORK .....</b>	<b>75</b>
	<b>REFERENCES .....</b>	<b>77</b>

## LIST OF TABLES

<b>Table</b>	<b>Page</b>
TABLE I: 0.3 Meter Offset Inflatable Aperture Antenna Geometrical Properties ...	30
TABLE II: Planar Near-Field Antenna Test Facility Properties .....	33
TABLE III: RF Pressurization Performance Comparison .....	51
TABLE IV: RMS Pressurization Performance Comparison .....	69
TABLE V: RF & Ruze Equation Performance Comparisons .....	70

## LIST OF FIGURES

<b>Figure</b>		<b>Page</b>
Figure 1:	Inflatable Antenna Experiment .....	8
Figure 2:	0.3 Meter Offset Inflatable Antenna .....	9
Figure 3:	4 x 6 Meter Offset Inflatable Antenna .....	10
Figure 4:	Hencky Curve Error .....	11
Figure 5:	Ideal Paraboloidal Antenna Surface Reflection .....	13
Figure 6:	Non-Ideal Paraboloidal Antenna Surface Reflection .....	15
Figure 7:	Aperture Divided into $N$ Hatbox Regions .....	18
Figure 8:	Aperture Divided into $N$ Hat Regions .....	20
Figure 9:	Ruze Loss Correction Factor .....	22
Figure 10:	0.3 Meter Offset Inflatable Aperture Antenna Installation .....	29
Figure 11:	0.3 Meter Antenna Geometry .....	30
Figure 12:	0.3 Meter Antenna Support Structure .....	31
Figure 13:	Planar Near-Field Antenna Test Facility .....	32
Figure 14:	0.3 Meter Antenna in Planar Near-Field Antenna Test Facility .....	34
Figure 15:	Leica 200 Photogrammetry System .....	35
Figure 16:	Coordinate Transformation Block Diagram .....	37

Figure 17:	Azimuth Far-Field Patterns, 0.000 inch H <sub>2</sub> O Pressurization .....	39
Figure 18:	Elevation Far-Field Patterns, 0.000 inch H <sub>2</sub> O Pressurization .....	40
Figure 19:	Azimuth Far-Field Patterns, 0.030 inch H <sub>2</sub> O Pressurization .....	41
Figure 20:	Elevation Far-Field Patterns, 0.030 inch H <sub>2</sub> O Pressurization .....	42
Figure 21:	Azimuth Far-Field Patterns, 0.040 inch H <sub>2</sub> O Pressurization .....	43
Figure 22:	Elevation Far-Field Patterns, 0.040 inch H <sub>2</sub> O Pressurization .....	44
Figure 23:	Azimuth Far-Field Patterns, 0.050 inch H <sub>2</sub> O Pressurization .....	45
Figure 24:	Elevation Far-Field Patterns, 0.050 inch H <sub>2</sub> O Pressurization .....	46
Figure 25:	Azimuth Far-Field Patterns, 0.060 inch H <sub>2</sub> O Pressurization .....	47
Figure 26:	Elevation Far-Field Patterns, 0.060 inch H <sub>2</sub> O Pressurization .....	48
Figure 27:	Azimuth Far-Field Patterns, 0.070 inch H <sub>2</sub> O Pressurization .....	49
Figure 28:	Elevation Far-Field Patterns, 0.070 inch H <sub>2</sub> O Pressurization .....	50
Figure 29:	Raw Photogrammetry Data, 0.000 inch H <sub>2</sub> O Pressurization .....	52
Figure 30:	Transformed & Ideal Paraboloid, 0.000 inch H <sub>2</sub> O Pressurization .....	53
Figure 31:	Raw Photogrammetry Data, 0.030 inch H <sub>2</sub> O Pressurization .....	55
Figure 32:	Transformed & Ideal Paraboloid, 0.030 inch H <sub>2</sub> O Pressurization .....	56
Figure 33:	Raw Photogrammetry Data, 0.040 inch H <sub>2</sub> O Pressurization .....	58
Figure 34:	Transformed & Ideal Paraboloid, 0.040 inch H <sub>2</sub> O Pressurization .....	59
Figure 35:	Raw Photogrammetry Data, 0.050 inch H <sub>2</sub> O Pressurization .....	61

Figure 36:	Transformed & Ideal Paraboloid, 0.050 inch H <sub>2</sub> O Pressurization .....	62
Figure 37:	Raw Photogrammetry Data, 0.060 inch H <sub>2</sub> O Pressurization .....	64
Figure 38:	Transformed & Ideal Paraboloid, 0.060 inch H <sub>2</sub> O Pressurization .....	65
Figure 39:	Raw Photogrammetry Data, 0.070 inch H <sub>2</sub> O Pressurization .....	67
Figure 40:	Transformed & Ideal Paraboloid, 0.070 inch H <sub>2</sub> O Pressurization .....	68

## **CHAPTER I**

### **INTRODUCTION**

The intention of this study is to determine whether or not the Ruze Equation for the degradation in directivity is appropriate for evaluating the directivity performance of inflatable aperture antennas. When evaluating the performance of inflatable aperture antennas, testing must be performed in an appropriate environment before an antenna can be considered for use on a space mission. The methodology to perform this testing would consist of placing the inflatable antenna in a thermal vacuum chamber in order to emulate the effects of the antenna's performance on a space mission. Testing must be conducted in a thermal vacuum chamber and not in a standard anechoic chamber because the inflatable antenna will undergo changes in its paraboloidal shape because of the effects from the coefficient of thermal expansion and solar flux variation experienced by the antenna in the space environment.

One limitation that exists to this proposed testing plan of the inflatable aperture antenna is that the thermal vacuum chamber does not contain any Near-Field or Far-Field testing chambers. However, since the thermal vacuum chamber does have windows, it is possible to perform a photogrammetry analysis of the surface of the inflatable antenna. After the photogrammetry analysis would be completed, a Root Mean Square (RMS)

surface error would be computed and utilized in the Ruze Equation. From the Ruze Equation, the test would provide information only on the loss in directivity.

### **1.1 Intended Purpose of Work**

The intention of this study is to examine the viability of using the Ruze Equation when evaluating inflatable aperture antennas. The Ruze Equation utilizes information on the RMS surface error of an antenna and the wavelength that the antenna will be operating at to determine the loss in directivity due to surface errors [23]. Commonly, the surface errors that exist on an antenna are thought of as phase errors. Geometrical optics states that rays originating from the feed of an antenna, placed at the focal point of the paraboloid, will travel to the antenna surface and reflect in the axial direction, such that the rays are parallel to each other at the aperture plane. Once these rays reach the aperture plane, they will have all traveled the same distance and the aperture will be a plane of constant phase [2].

However, when there are surface errors, there can be a change in the direction that the reflected ray will travel, which can also change the phase of the ray when the ray reaches the aperture plane. Snell's Law states that the incident and reflection angles from the surface normal will be equal [2]. Surface errors will cause a change in the direction that the surface normal vector will be pointing, and therefore change the direction that the reflected ray will travel. In perfect paraboloid antennas, the surface normal can be easily determined from the equation of the paraboloid. However, when the antenna no longer

maintains the perfect paraboloidal shape, the surface normal vector direction will be modified from the ideal surface normal vector. If the errors in the antenna surface are such that the incident angle on the antenna surface is decreased from the ideal incident angle, the reflecting rays will be propagated in a direction that is not parallel to the axial direction. The reflected rays will thus have a smaller radial distance from the feed in the aperture plane. However, if the errors in the antenna surface are such that the incident angle on the antenna surface is increased from the ideal incident angle, the reflection rays will have a larger radial distance from the feed in the aperture plane. The changes in the direction of the reflected rays will also cause a change in distance that the reflected ray must be propagated. Phase errors are also introduced because of this reflection angle error.

The above effect is what creates errors in the phase front on the aperture plane. Rays will not travel in the appropriate direction, which is parallel to the axial direction of the antenna. The distance that the rays travel will be modified and the phase of the particular ray will be in error. The Ruze Equation attempts to characterize these effects and determine the degradation of the directivity of the antenna based on the RMS surface error and the wavelength that the antenna is operating at.

The methodology of this study consists of performing an RF scan in a Near-Field antenna testing range to determine the directivity and beam patterns of an offset inflatable aperture antenna. Concurrently, laser ranging scans will be performed to determine the RMS surface error to be used in the Ruze Equation. Both of these tests were performed on the inflatable aperture antenna while under multiple pressurizations, from which cases with wrinkles and cases where over-inflation exists can be examined. Directivity

measurements from the RF scan will be compared with the predicted directivity with known inefficiencies of the antenna. This will determine the additional loss that exists due to the surface errors of the inflatable antenna. The Ruze Equation will be utilized to determine the predicted surface error loss. Comparisons will then be made regarding the differences between the RF scan derived surface error loss with the surface error loss that the Ruze Equation predicts. This study will determine if these types of errors will not prohibit the Ruze Equation to be an accurate procedure of determining the loss in directivity for inflatable aperture antennas.

## **1.2 Background Introduction**

The Ruze Equation makes assumptions about the nature of the surface errors. The Ruze Equation assumes that the surface errors are random in nature and that they are uncorrelated to each other [23]. The Ruze Equation also assumes that the errors on the antenna surface are of the nature of a Gaussian probability density function. Inflatable aperture antennas have more than random surface errors present on the antenna surface. These errors, called the W-curve errors, create a non-paraboloidal shape at the edges of the inflatable antenna surface and a spherical aberration near the vertex [4]. This causes many errors to be created near the edge of the antenna. The W-curve errors also create a change in the shape of the paraboloidal portion of the inflatable antenna which can be characterized as the focal point of the paraboloid no longer being at the same location as the feed of the antenna. Other errors that can exist on an inflatable antenna include those caused from improper inflation of the antenna. The inflatable antenna could be over-

inflated and cause a change in the ideal focal point of the paraboloid, or the inflatable antenna could be under-inflated and wrinkles could form on the antenna surface, creating additional surface errors.

### **1.3 Chapter Topics**

Chapter Two will give further background information on inflatable antennas. The Ruze Equation will be discussed in detail, along with how it originated. The appropriate calculation for the RMS surface errors will be discussed. Finally surface sampling requirements for an appropriate photogrammetry study will be identified based on the Nyquist Sampling Theorem.

Chapter Three will include information on the multiple testing equipment/routines that were utilized in the analysis for this study. Information on the particular offset inflatable aperture antenna will be provided. The Near-Field RF scanning equipment will be discussed. The equipment that was used to perform the photogrammetry study will be presented along with known errors of the equipment. Finally, the Matlab software routine that was used to transform the photogrammetry data to an appropriate coordinate system, for use in calculating the RMS surface error, will be presented.

Chapter Four will present results of the tests performed on the offset inflatable aperture antenna for the different pressurization levels. Detailed directivity and beam pattern results will be presented from the Near-Field RF scans. The transformed

photogrammetry data will be presented and compared with ideal paraboloidal data. The RMS surface error will be calculated. Finally, comparisons will be made between the surface error loss exhibited in the RF scans on the antenna and what is predicted from the Ruze Equation.

Chapter Five will review the performance of the inflatable aperture antenna and summarize all of the results that were reached in Chapter Four. The viability of the Ruze Equation when working with inflatable antennas which have errors that are not characterized by the Ruze Equation will be noted as well.

Chapter Six will provide information on future work in this area. Plans will be addressed about computing the secondary beam pattern information and directivity from the photogrammetry study. The methodology to evaluate the surface normal vector and the reflected ray when errors exist on the antenna surface will be presented. The concept of a possible study concerning the sag effect on the antenna which is due to gravity will be introduced. Plans will be discussed for possible testing of a one meter diameter inflatable aperture antenna. Finally, a brief discussion is provided on the topic of the creation of a more comprehensive equation that would accurately describe the directivity degradation for inflatable aperture antennas.

## **CHAPTER II**

### **BACKGROUND INFORMATION**

Chapter Two will give further detailed information on inflatable antennas, the Ruze Equation, RMS errors, and Nyquist surface sampling requirements. An overview of inflatable antennas will be provided in Section 2.1 including information on the benefits, limitations, and illustrations of those antennas. In Section 2.2, the Ruze Equation will be explained in detail. Illustrations of surface errors and their effect on the aperture phase front will also be provided. Section 2.3 will provide information regarding the calculation of the RMS surface error. Finally, Section 2.4 will discuss surface sampling requirements for an appropriate photogrammetry study derived from requirements of the Nyquist Sampling Theorem.

#### **2.1 Inflatable Aperture Antennas**

Inflatable aperture antennas are an emerging research technology that provides several advantages over standard reflector antenna systems. Inflatable aperture antennas can provide benefits in terms of size and density and are designed such that they can be

packed into a small stowage space and inflated to full-size at a later time [26]. They are designed to be inflated to the designed paraboloidal shape, which would be held in place by some form of structural supports. Inflatable aperture antennas need an inflation system to be present, which is not necessary for standard parabolic reflector antennas. The aerial density of inflatable aperture antennas that have been developed has been lower than  $1 \text{ kg/m}^2$  [26].

There has been only one inflatable aperture antenna flown in space to date. The antenna was the 14 meter Inflatable Antenna Experiment (IAE) that was launched aboard the Space Shuttle Endeavor - Mission STS-77 in 1996. Figure 1 shows an image of the IAE as viewed from the Space Shuttle Endeavor [26].



Figure 1: Inflatable Antenna Experiment

The experiment lasted 90 minutes, during which the antenna support structure was successfully deployed to the proper shape. However, the lens shaped reflector failed to

inflate. This failure meant that there were no in-flight measurements regarding the surface accuracy of the inflatable aperture antenna [26].

Several inflatable aperture antennas have been under investigation at NASA Glenn Research Center since 2004. NASA Glenn Research Center has been partnering with SRS Technologies, which has manufactured several inflatable aperture antennas, including a 0.3 meter offset inflatable antenna [12, 18, 19, 22, 26] and a 4 x 6 meter offset inflatable antenna [26]. The 0.3 meter offset inflatable antenna, which is shown in Figure 2, was tested at 8.4 GHz. The performance of the antenna was comparable to a similar size conventional rigid reflector antenna and also performed well compared to the theoretical predictions [12, 18, 19, 22, 26].



Figure 2: 0.3 Meter Offset Inflatable Antenna

A 4 x 6 meter offset inflatable antenna was also manufactured by SRS Technologies. This antenna is inflated in the aperture and in the torus which is used to support the aperture. The 4 x 6 meter offset inflatable antenna, shown in Figure 3 inside the NASA Glenn Research Center Near-Field test facility, was tested and characterized at 8.4 GHz and 32 GHz [26].



Figure 3: 4 x 6 Meter Offset Inflatable Antenna

Measured directivities were 49.4 dBi and 51.6 dBi, which corresponded to efficiencies of 71% at 8.4 GHz and 8% at 32 GHz [26]. An RMS surface error was measured for this antenna and was computed to be 3.5 mm. According to the Ruze Equation, this amount of surface error would lead to much greater gain degradation at the Ka-band frequency of 32 GHz (i.e. 99 dB). Phase plots of the near field data show macroscopic surface errors,

which contribute to the gain degradation, but also show that some of the surface errors are not independent of each other.

One of the main limitations of inflatable aperture antennas that have been under much investigation is their inability to overcome the non-ideal paraboloidal shape known as the Hencky curve. The Hencky curve, also known as the “W-curve” is an attribute of inflatable structures involving the amount of strain on the surface of the walls of the structure which produces an ill-shaped paraboloid [4]. The ill-shaped paraboloid produces what is called spherical aberration in the reflected fields. The Hencky curve prevents an inflatable structure from achieving a paraboloidal shape. The result of the Hencky curve is that the boundary edge of the reflector will be spread out compared to how an ideal paraboloid should be. This is illustrated in the graph in Figure 4 [4], in which  $a$  is the radius of the antenna and  $r$  is the radial distance variable for the antenna.

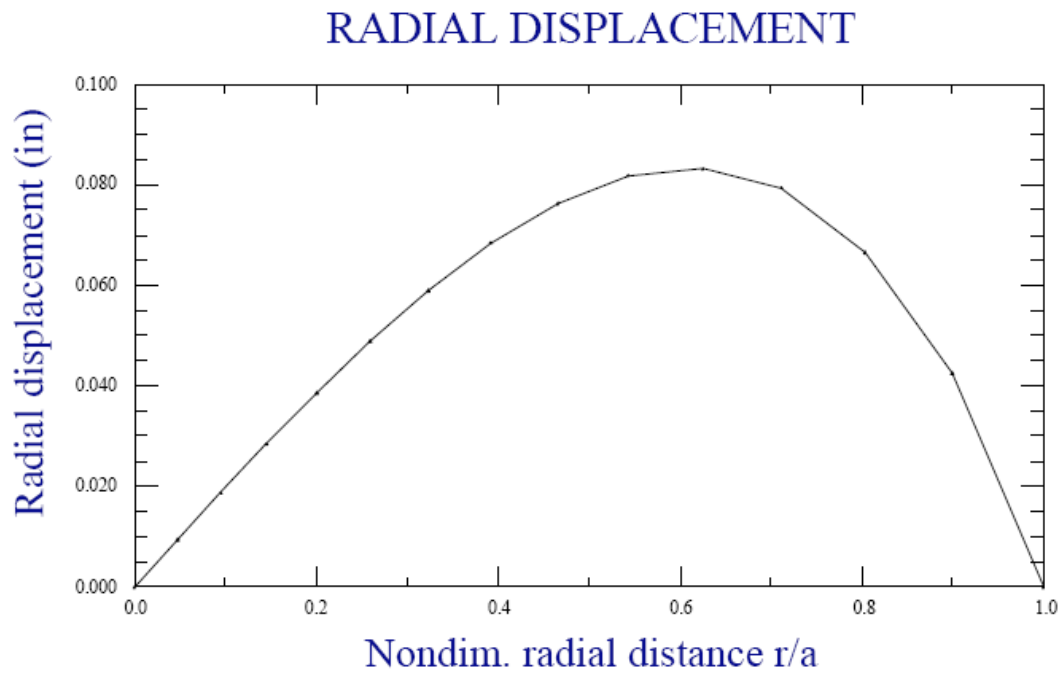


Figure 4: Hencky Curve Error

As the graph shows, the only locations of an ideal surface may be located at the vertex or at the edge boundary of the inflatable aperture antenna, shown at the left and right sides of the graph. The effect of the Hencky curve is that the antenna begins to become too steep too early, in regards to its slope away from the vertex. As the membrane structure reaches the edge boundary, the surface spreads out until the boundary is reached. Another way to understand the effects of the Hencky curve is to recognize that the design focal point will no longer be at the location of the ideal focal point. Techniques to control this effect have shown to be somewhat effective. These techniques include fabricating the inflatable aperture reflectors with electroactive polymers [4], performed by the California Institute of Technology Jet Propulsion Laboratory, and placing structures around the edge boundary of the reflector to help control the shape accuracy [13, 14].

## **2.2 Ruze Theory**

The surface errors that exist on an antenna are thought of as phase errors, because surface errors cause the phase front at the aperture plane to fluctuate. An example of an ideal paraboloidal antenna surface reflection ray is illustrated in Figure 5. For an antenna operating in transmit mode, geometric optics states that rays originating from the feed of an antenna travel to the antenna surface and are reflected traveling parallel to the axial direction of the antenna. All of the rays are thought of as being parallel when dealing with an ideal paraboloidal surface. Once these rays reach the aperture plane, they would

have all traveled the same distance and the aperture would be a plane of constant phase [4].

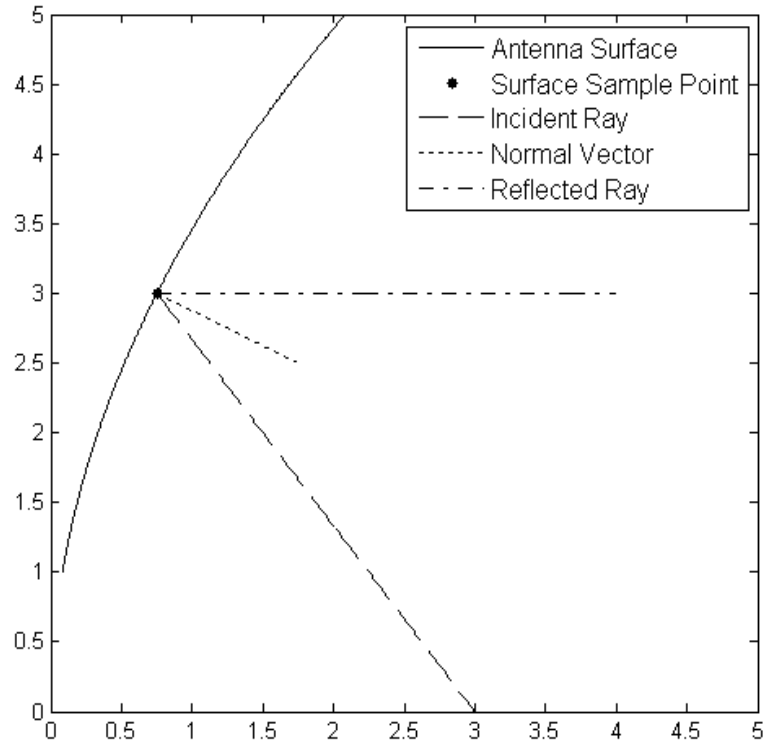


Figure 5: Ideal Paraboloidal Antenna Surface Reflection

In Figure 5, the dashed line shows the ray that originates from the feed, at the focal point location, which travels to the antenna surface. The antenna surface, shown as the solid line, is that of an ideal paraboloid. The dotted line denotes the normal vector at the point of reflection on the antenna surface. Finally, the dashed-dotted line illustrates the ray reflecting off of the antenna surface and traveling parallel to the axial direction, defined as the x-axis of the plot.

However, when there are surface errors, there can be a change in the direction that the reflected ray will travel, which can also change the phase of the ray when the ray reaches the aperture plane. Snell's Law states that the incident and reflection angles from the surface normal will be equal [4]. Surface errors will cause a change in the direction that the surface normal vector will be pointing, and therefore change the direction that the reflected ray will travel. Figure 6 shows an illustration of this effect for a non-ideal paraboloidal surface. Despite what type of surface errors exist, Snell's Law must be true. Therefore, even when the antenna no longer maintains the perfect paraboloidal shape, the incident and reflection angles from the surface normal must still be equal. The result is that the reflected rays will no longer travel in the direction parallel to the axial direction of the antenna. The changes in the direction of the reflecting rays will also cause a change in distance that the reflecting ray must be propagated, thus phase errors are also introduced because of this reflection angle error from the ideal.

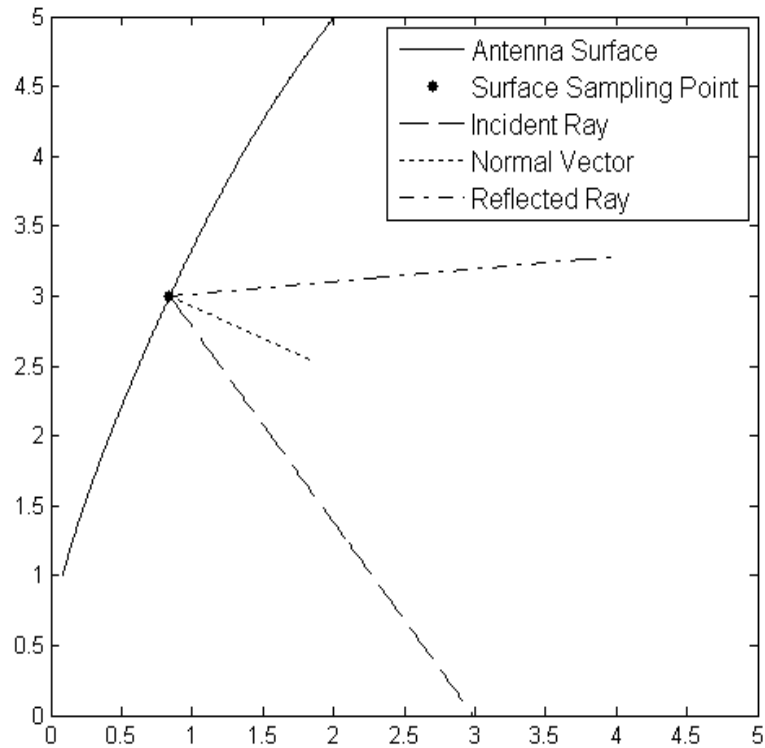


Figure 6: Non-Ideal Paraboloidal Antenna Surface Reflection

In Figure 6, the line types have the same meaning in regards to antenna surface, incident ray, normal vector, and reflected ray as in Figure 5, except that the solid line is of the corrupted antenna surface and the reflected ray is traveling in the non-ideal direction, compared to the direction in which it would travel in the ideal paraboloidal case. This above effect is what creates errors in the phase front on the aperture plane. Rays do not travel in the appropriate direction, which is parallel to the axial direction of the antenna. The distance that the rays travel will be modified and the phase of the particular ray will be in error.

The Ruze Equation attempts to understand these effects and determine the degradation of the directivity of the antenna based on the surface RMS value and the wavelength that the antenna is operating at [23]. The derivation of the Ruze Equation can be found in [23]. The Ruze Equation was derived from a first principles methodology. Ruze states that the axial gain of a circular antenna with a phase error can be defined as such, in Equation 1.

$$G = \frac{4\pi}{\lambda^2} \frac{\left| \int_0^{2\pi} \int_0^a f(r, \phi) e^{j\delta(r, \phi)} r dr d\phi \right|^2}{\int_0^{2\pi} \int_0^a f^2(r, \phi) r dr d\phi} \quad (1)$$

In Equation 1, the terms used are defined as follows:

- $G$  is the axial gain of the antenna
- $\lambda$  is the wavelength that the antenna is operating at
- $r, \phi$  are the aperture coordinates
- $f(r, \phi)$  is the in-phase illumination function in terms of the aperture coordinates
- $\delta(r, \phi)$  is the phase error in terms of the aperture coordinates

Making the assumption that the phase errors are small, the exponential in the numerator of Equation 1 can be expanded into a power series. When the ratio of the gain, with errors, is taken to the gain with zero errors, this ratio can be approximated as Equation 2.

$$\frac{G}{G_0} \approx 1 - \overline{\delta^2} + \overline{\delta^4} \quad (2)$$

In Equation 2, the additional terms used are defined as follows:

- $G_0$  is the axial gain of the antenna without phase error  $\eta(\pi D / \lambda)^2$
- $\lambda$  is the wavelength that the antenna is operating at
- $D$  is the diameter of the antenna
- $\eta$  is the known efficiency of the antenna
- $\overline{\delta^2}$  is the weighted mean-square phase error
- $\overline{\delta}$  is the illumination weighted mean phase error

The mean phase error and illumination weighted mean phase error are defined by Equations 3 and 4, respectively.

$$\overline{\delta^2} = \frac{\int_0^{2\pi} \int_0^a f(r, \phi) \delta^2(r, \phi) r dr d\phi}{\int_0^{2\pi} \int_0^a f(r, \phi) r dr d\phi} \quad (3)$$

$$\overline{\delta} = \frac{\int_0^{2\pi} \int_0^a f(r, \phi) \delta(r, \phi) r dr d\phi}{\int_0^{2\pi} \int_0^a f(r, \phi) r dr d\phi} \quad (4)$$

Note that the difference between the terms in Equations 3 and 4 is that the phase error term used in the numerator of Equation 3 is squared, while in Equation 4 the term is to the power of one. If the phase reference plane is chosen such that  $\overline{\delta}$ , the illumination weighted mean phase error, is set to zero, then Equation 2 reduces to Equation 5 as follows.

$$\frac{G}{G_0} \approx 1 - \overline{\delta_0^2} \quad (5)$$

The relationship provided in Equation 5 shows that the loss in gain due to phase errors is equal to the weighted mean-square phase error. This relationship is valid for any type of surface error pattern present on any antenna. The next step that Ruze took in development of his equation was to extend the previous equation for the case of large phase errors. Ruze did not have detailed knowledge of the phase front error, so he had to utilize the statistical properties of the surface error.

Ruze began his advanced analysis by separating the aperture into  $N$  regions. Each region, which Ruze called a “hat box” due to the constant amplitude over the circular region, has a phase error and is not related to any neighboring regions. The axial field can be assumed to be the sum of the individual contributions from all of the  $N$  regions. An illustration of this is shown in Figure 7, in which  $c$  is the radius of one of the  $N$  correlation regions.

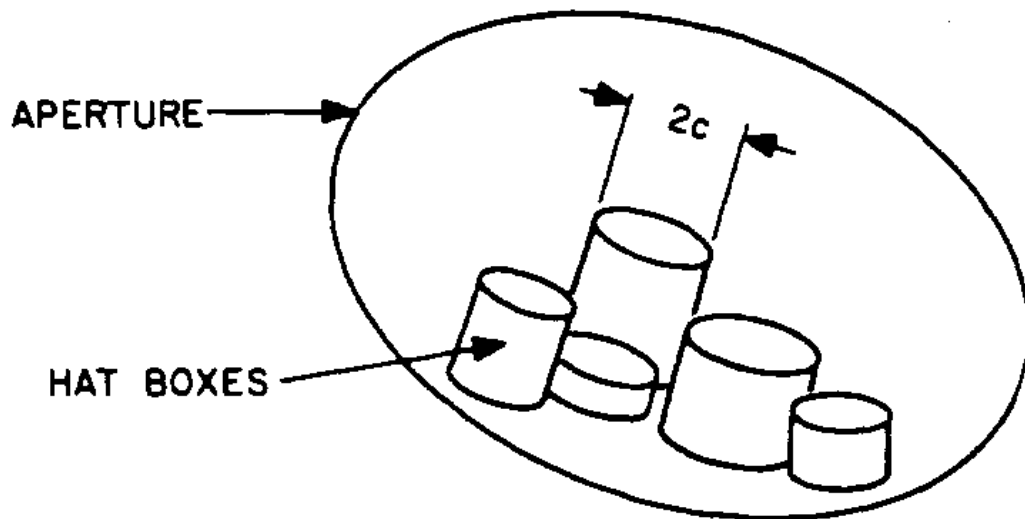


Figure 7: Aperture Divided into  $N$  Hatbox Regions

If there are  $N$  unit field vectors with zero phase error, then the power sum can be derived as  $N^2$ . However, since there are phase errors, if it is assumed that the phase errors are Gaussian in nature with variance  $\overline{\delta^2}$  in radians, then the power sum can be expressed as in Equation 6.

$$\overline{P} = N^2 e^{-\overline{\delta_N^2}} + N \left( 1 - e^{-\overline{\delta_N^2}} \right) \quad (6)$$

In Equation 6, the additional terms used are defined as follows:

- $\overline{P}$  is the power sum
- $\overline{\delta_N^2}$  is the variance of the phase error

The expected radiation pattern of the model shown in Figure 7 can also be derived. First, it must be assumed that the phase values are correlated in a diameter of  $2c$ , where  $2c$  is the diameter of the regions, known as hatboxes, shown in Figure 7. Phase values are uncorrelated for distances larger than  $2c$ . Also, as before, the phase errors are of a Gaussian distribution with variance  $\overline{\delta_N^2}$  in radians. Finally, the number of regions must be large enough to satisfy the following relationship, in Equation 7.

$$N \approx \left( \frac{D}{2c} \right)^2 \gg 1 \quad (7)$$

From these assumptions, the expected radiation pattern in the far-field can be derived as such, in Equation 8.

$$G(\theta, \phi) = G_0(\theta, \phi) e^{-\overline{\delta_N^2}} + \left( \frac{2\pi c}{\lambda} \right)^2 \left( 1 - e^{-\overline{\delta_N^2}} \right) \Lambda_1 \left( \frac{2\pi c \sin \theta}{\lambda} \right) \quad (8)$$

In Equation 8, the additional terms used are defined as follows:

- $\theta, \phi$  are the far-field coordinates
- $\Lambda_1(\ )$  is the Lambda function

Equation 8 shows a similarity to Equation 6, in that zero-error radiation diagram is reduced by an exponential term. Also, a scattered field is added which has a beamwidth that is inversely proportional to the radius of the correlated regions. Equation 8 can be improved if the hatboxes, shown in Figure 7, are replaced with hats, shown in Figure 8.

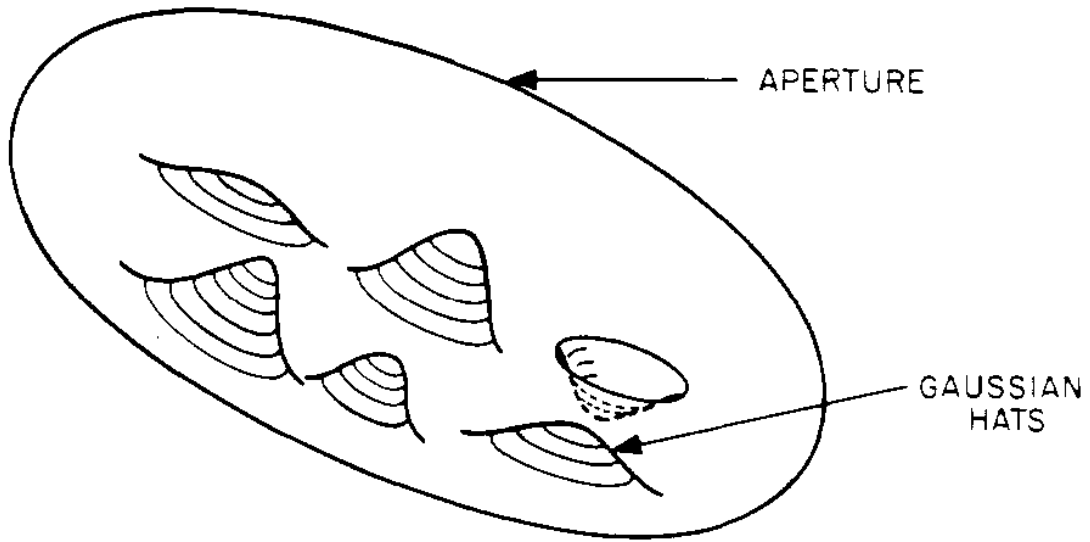


Figure 8: Aperture Divided into  $N$  Hat Regions

If the phase front errors are assumed to have a Gaussian shape, the expected radiation pattern can be evaluated and defined in Equation 9.

$$G(\theta, \phi) = G_0(\theta, \phi) e^{-\overline{\delta_N^2}} + \left( \frac{2\pi c}{\lambda} \right)^2 e^{-\overline{\delta_N^2}} \sum_{n=1}^{\infty} \frac{\overline{\delta_N^2}^n}{n \cdot n!} e^{-\left( \frac{\pi c \sin \theta}{\lambda} \right)^2 / n} \quad (9)$$

Equation 9 can be modified to express the reduction in the axial gain, which is shown in Equation 10.

$$\frac{G}{G_0} = e^{-\overline{\delta_N^2}} + \frac{1}{\eta} \left( \frac{2c}{D} \right)^2 e^{-\overline{\delta_N^2}} \sum_{n=1}^{\infty} \frac{\overline{\delta_N^2}^n}{n \cdot n!} \quad (10)$$

For correlation regions that are small compared to the antenna diameter, the second term of Equation 10 can be ignored to produce Equation 11.

$$G = \eta \left( \frac{\pi D}{\lambda} \right)^2 e^{-\left( \frac{4\pi\varepsilon}{\lambda} \right)^2} \quad (11)$$

In Equation 11, the additional term used is defined as follows:

- $\varepsilon$  is the RMS surface error of the antenna

Since the directivity of an antenna with zero error is known as  $\eta(\pi D / \lambda)^2$ , the loss due to surface errors can be represented as follows in Equation 12, known as the Ruze Equation.

$$L_R = e^{-\left( \frac{4\pi\varepsilon}{\lambda} \right)^2} \quad (12)$$

In Equation 12, the additional term used is defined as follows:

- $L_R$  is the loss in directivity due to surface errors

Ruze found through experimentation, that the surface error directivity loss was too large by a factor of  $A$  [23]. This factor was determined by the methodology that the surface errors were computed and the depth of the antenna. Surface errors could be calculated from axial errors or normal errors. The depth of the antenna is defined by the

ratio of the focal length to the diameter of the antenna,  $f/D$ . The curves that define the term  $A$  are shown in Figure 9 [23]. Equation 13 shows the modified Ruze Equation.

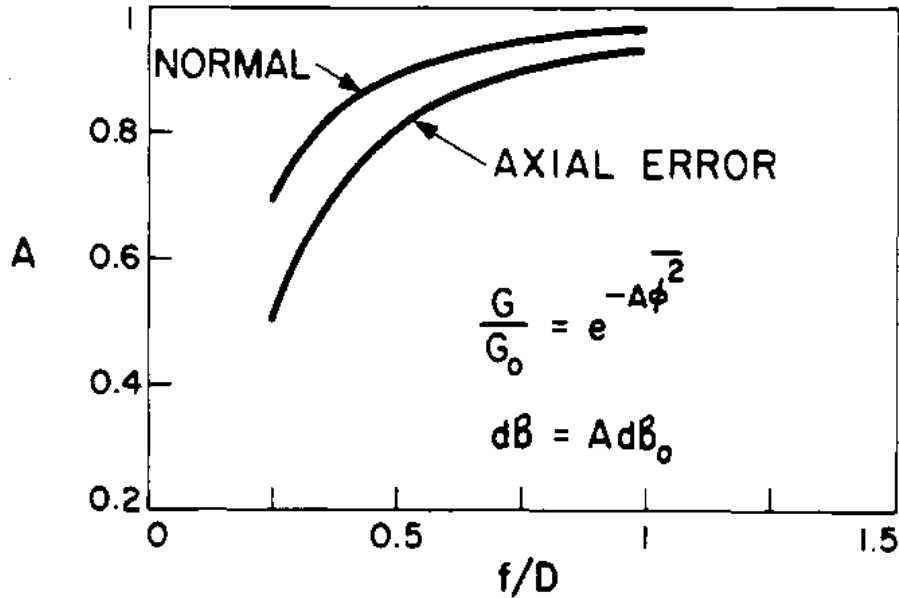


Figure 9: Ruze Loss Correction Factor

$$L_R = e^{-A\left(\frac{4\pi\varepsilon}{\lambda}\right)^2} \quad (13)$$

In Equation 13, the additional term used is defined as follows:

- $A$  is the Ruze loss correction factor

The final topic of discussion of the Ruze theory involves the limitations of the Ruze Equation. These limitations are based on assumptions that were made during the derivation regarding the statistical estimates of the phase errors that are present for the antenna. Five distinct assumptions are noted by Ruze [23].

1. The surface errors on the antenna are random in nature.

2. The surface errors are uniformly distributed over the aperture.
3. The surface errors are distributed in fixed, circular correlation regions.
4. The aperture of the antenna is much larger compared to the diameter correlation region,  $D \gg 2c$
5. The surface errors have a Gaussian spatial phase correlation.

The believed limitations of the Ruze Equation regarding usage for inflatable aperture antennas can be looked at regarding the above assumptions. First, surface errors on inflatable aperture antennas come from the errors associated with the Hencky curve and due to wrinkles caused from improper inflation of the aperture. Second, the surface errors of inflatable aperture antennas may not be uniformly distributed over the aperture due to the location that wrinkles typically occur at. Finally, the surface errors are not distributed in fixed, circular correlation regions due to the nature of the errors associated with the Hencky profile. It can be established from these conclusions that the Ruze Equation may not be applicable to inflatable aperture antennas.

### **2.3 RMS Error Calculation**

The accuracy of a surface compared to an ideal version of the surface can be computed via the RMS of the surface error. The RMS of the surface error is a parameter that is used in the Ruze Equation to compute the predicted loss in directivity due to errors on the surface of an antenna. The most accurate RMS error is computed from the error

between continuous functions of the actual and ideal antenna surfaces [29]. This RMS error equation is shown below in Equation 14.

$$\varepsilon = \sqrt{\frac{1}{S} \iint_S e^2(x, y) dx dy} \quad (14)$$

In Equation 14, the additional terms used are defined as follows:

- $S$  is the area of the antenna surface
- $e$  is the continuous error between actual and ideal antenna surfaces
- $x, y$  are the antenna coordinates from which error is measured

It is important to note that  $\varepsilon$  is not the square root of a variance, but rather a deterministic quantity originating from the error from the actual shape of an antenna. Equation 14 assumes that the actual surface is known in the form of a continuous function. Since the actual surface is not known in the form of a continuous function, but rather from a discrete set of data points, the measurement error also needs to be taken into account. Equation 15 is an approximation of the continuous RMS surface error for  $M$  discrete points measured on the antenna surface that also takes the measuring device error into account [29].

$$\varepsilon = \sqrt{\frac{1}{M} \sum_{i=1}^M (\xi_i + \Delta z_i)^2} \quad (15)$$

In Equation 15, the additional terms used are defined as follows:

- $M$  is the number of discrete antenna surface points
- $\xi_i$  is the random measuring equipment induced error

- $\Delta z_i$  is the deterministic error between the actual and ideal antenna surface

However, when  $\varepsilon \gg \sigma$ , where  $\sigma$  is the standard deviation of the measuring equipment error, the dominant term of the error is the deterministic error between the actual and ideal antenna surfaces. Therefore, the random measuring equipment induced error can be neglected, as such, in Equation 16, which is used later to compute RMS surface accuracies.

$$\varepsilon = \sqrt{\frac{1}{M} \sum_{i=1}^M (\Delta z_i)^2} \quad (16)$$

## 2.4 Antenna Surface Sampling Requirements

Surface sampling of discrete antenna points is dictated by the Nyquist sampling rate. The Nyquist sampling theorem requires that a function have a spectrum that exists and is non-vanishing over the finite region of wave-number space [1]. Under the completion of these two requirements, the function may be exactly reproduced when the function is sampled on a periodic grid at a rate of at least two times the maximum frequency. The minimum number of points necessary in a single dimension can be derived in Equation 17 for the x-dimension and Equation 18 in the y-dimension, assuming that the data will be analyzed over the z-dimension.

$$N_x = \left\lceil \frac{2L_x}{\lambda} \right\rceil + 1 \quad (17)$$

$$N_y = \left\lfloor \frac{2L_y}{\lambda} \right\rfloor + 1 \quad (18)$$

In Equation 17 and Equation 18, the additional terms used are defined as follows:

- $N_x$  is the minimum number of sampling points in the x-dimension
- $N_y$  is the minimum number of sampling points in the y-dimension
- $L_x$  is the length of the antenna in the x-axis
- $L_y$  is the length of the antenna in the y-axis
- $\lfloor \cdot \rfloor$  is the floor function

If the antenna aperture were rectangular in nature, then the minimum number of sampling points over the antenna surface would be  $N_x N_y$ . However, since the inflatable aperture antenna is circular in nature, the minimum number of sampling points in the x-dimension is equal to the minimum number of sampling points in the y-dimension. Therefore, the total minimum number of sampling points is the area of the antenna divided by the area of a sampling point and is defined by Equation 19.

$$N_M = \left\lfloor \frac{\pi D^2}{\lambda^2} \right\rfloor + 1 \quad (19)$$

In Equation 19, the additional term used is defined as follows:

- $N_M$  is the minimum number of sampling points

The minimum number of sampling points over the aperture is defined by Equation 19. However, there may be cases in which it is necessary to over-sample the antenna

surface. This may be due to known wrinkles which have a high spatial frequency. This may also be due to a desire to examine microscopic surface errors. A limitation that may exist for inflatable aperture antennas is a non-constant antenna surface over the duration of the scanning period. If this is the case, the number of sampling points should be kept near the Nyquist sampling minimum.

## **CHAPTER III**

### **EQUIPMENT AND METHODOLOGY**

Chapter Three will document the various testing instruments and analysis routines that were utilized in the analysis for this study. Section 3.1 provides information on the 0.3 meter offset inflatable aperture antenna. The Near-Field RF scanning equipment will be discussed in Section 3.2. Section 3.3 discusses the equipment that was used to perform the photogrammetry study, along with information on the known errors of the equipment. Finally, Section 3.4 explains the Matlab software routine that was used to transform the photogrammetry data to an appropriate coordinate system for use in calculating the RMS surface error.

#### **3.1 Offset Inflatable Reflector Antenna Specifications**

The antenna that was under testing for the purpose of this study was a 0.3 meter offset inflatable aperture reflector antenna. The antenna was manufactured by SRS Technologies and began various tests at NASA Glenn Research Center in 2004 [18]. The antenna was tested at various pressurization levels for the purpose of creating various

levels of surface errors. The antenna was tested at pressurizations of 0.00, 0.03, 0.04, 0.05, 0.06, and 0.07 inches H<sub>2</sub>O of ambient air. An illustration of the 0.3 meter offset inflatable aperture antenna being installed in the Far-Field Test Facility from 2004 is shown in Figure 10.



Figure 10: 0.3 Meter Offset Inflatable Aperture Antenna Installation

The antenna was tested at 8.4 GHz with a feed installed that utilized an 11 dB taper, creating a known efficiency of 0.68. Parameters of the geometry of the antenna are listed below in Table I [18].

**TABLE I:** 0.3 Meter Offset Inflatable Aperture Antenna Geometrical Properties

Property	Value
Diameter	0.3048 meter
Wavelength	0.0357 meter at 8.4 GHz
Focal Length	0.152 meter
Focal Length/Diameter	0.5
Offset Distance	2.54 cm
Depth	3.8 cm
Major Length	0.353 meter
Tilt Angle	52.05°
Half Cone Angle	42.53°
Slope Angle	59.74°

An illustration of the side profile of the antenna is shown in Figure 11.

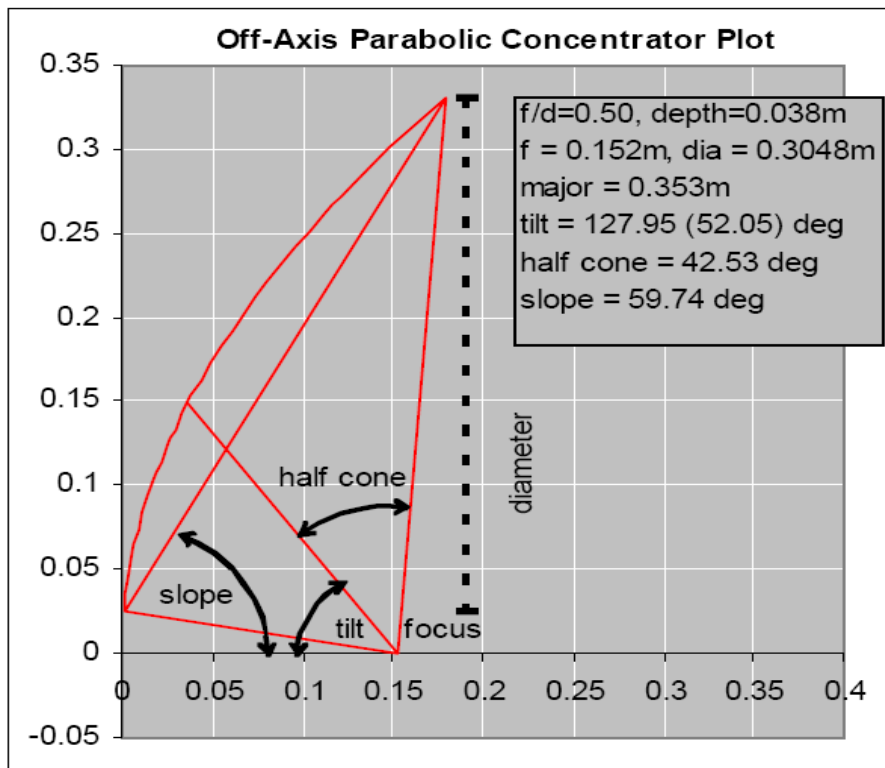


Figure 11: 0.3 Meter Antenna Geometry

Finally, Figure 12 shows a graphic of the design of the antenna with its support structure.

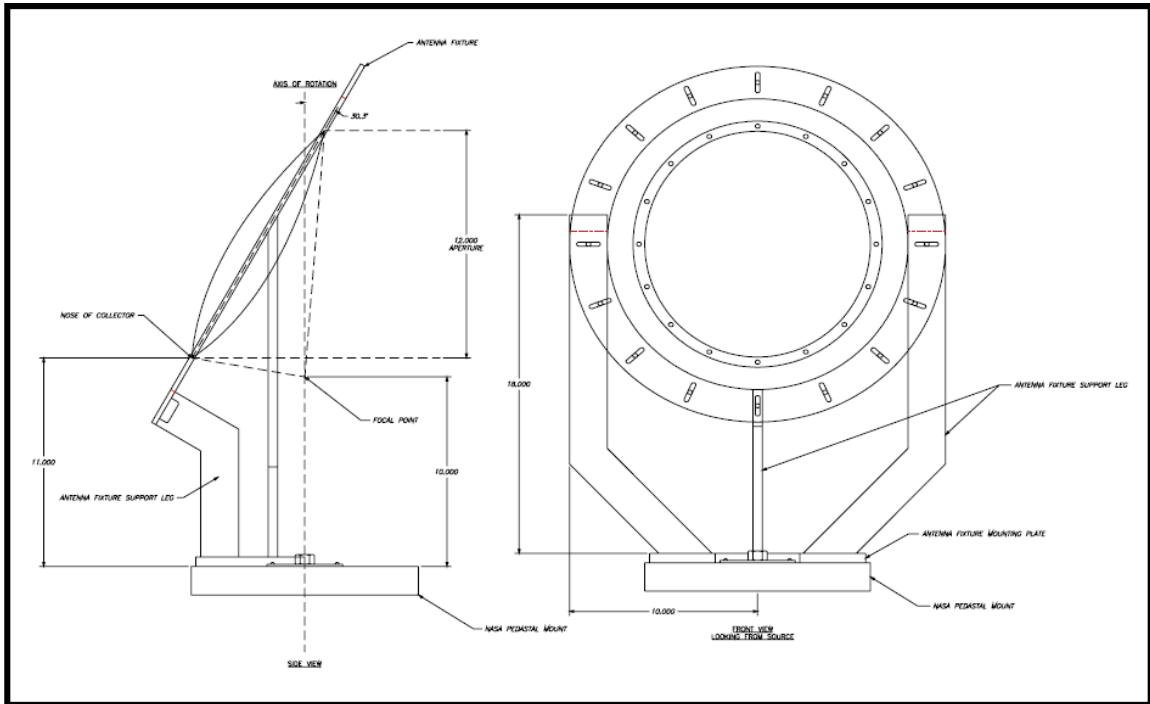


Figure 12: 0.3 Meter Antenna Support Structure

### 3.2 Planar Near-Field Antenna Test Facility

NASA Glenn Research Center operates a Planar Near-Field Antenna Test Facility that has capabilities to measure electromagnetic radiation characteristics of antenna systems and components to support development of advanced antenna technologies for commercial communications systems and NASA missions. An image of the Planar Near-Field Antenna Test Facility is provided in Figure 13.

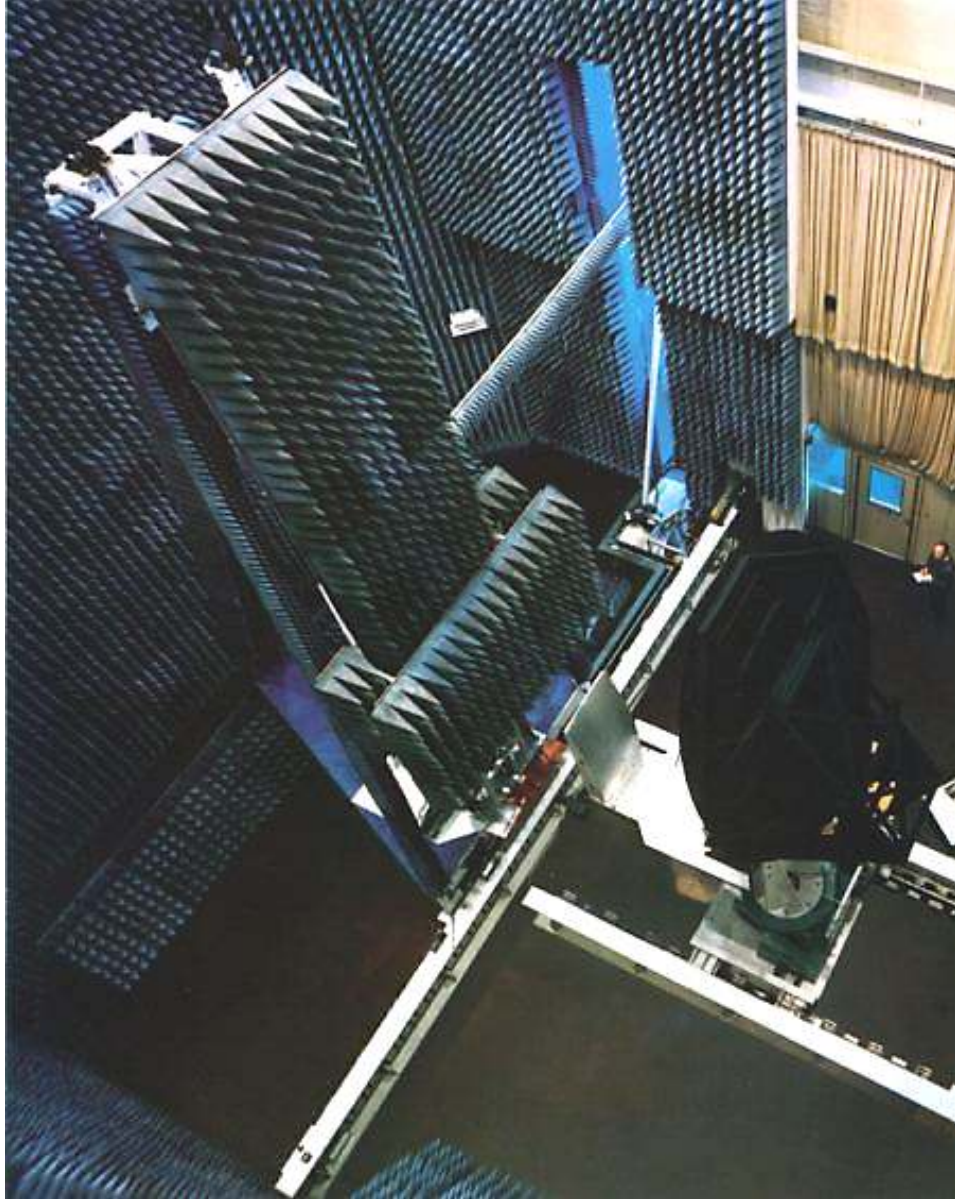


Figure 13: Planar Near-Field Antenna Test Facility

Properties of the Planar Near-Field Antenna Test Facility are listed in Table II.

**TABLE II:** Planar Near-Field Antenna Test Facility Properties

<b>Property</b>	<b>Value</b>
Frequency Range	1 to 40 GHz
Scanning Plane	22 x 22 ft
Positioning & Alignment Method	Laser
Dynamic Range	80 dB
Antenna Size	Up to 15 ft Diameter
Scanning Plane Flatness	0.004 inch RMS

The Planar Near-Field Antenna Test Facility was utilized to measure the electromagnetic fields of the 0.3 meter offset inflatable aperture antenna at a frequency of 8.4 GHz. Vertical and horizontal polarization measurements will be taken to compute the co-polarization and cross-polarization fields. Measurements will be taken under all six antenna inflation pressurizations. Figure 14 shows an image of the 0.3 meter offset inflatable aperture antenna on the pedestal of the Planar Near-Field Antenna Test Facility prior to testing.



Figure 14: 0.3 Meter Antenna in Planar Near-Field Antenna Test Facility

### 3.3 Leica 200 Photogrammetry System

The Leica 200 Photogrammetry System was utilized to perform a photogrammetry study of the surface of the 0.3 meter inflatable aperture antenna. The

Leica 200 utilizes laser ranging measurements with known pointing angles to determine the location of the object being measured. Figure 15 shows an image of the Leica 200 Photogrammetry System in the Planar Near-Field Antenna Test Facility.



Figure 15: Leica 200 Photogrammetry System

The Leica 200 Photogrammetry System has an expected error on the order of  $\pm 25$   $\mu\text{m}$ . However, there are occasions where false measurements are made. To fix this issue, the Leica 200 Photogrammetry System comes with a software package called CloudViewer. The CloudViewer software package allows the user to view the measured points and delete erroneous data points. Sampling distance is an input to the laser ranging metrology scan procedure. Sampling distance was set at 0.1 inches, in order to

try to visualize macroscopic errors such as the Hencky curve and wrinkles, as well as some microscopic errors that the Ruze Equation attempts to characterize.

### 3.4 Data Transformation Routine

Data points obtained from the photogrammetry study are not necessarily in the proper coordinate system that the ideal paraboloid would be known in. Therefore, the data points need to be transformed into the proper coordinate system. The proper coordinate system is one in which the antenna points along the z-axis and the vertex of the antenna is located at the origin of the coordinate system. The focal point of the antenna would be located in the location of  $(0, 0, f)$ , in which the points refer to the Cartesian triplet  $(x, y, z)$  and  $f$  is the focal length for the paraboloid. The routine for the transformation is performed in Matlab computer software [19]. The algorithm is based on details in the following block diagram, in Figure 16.

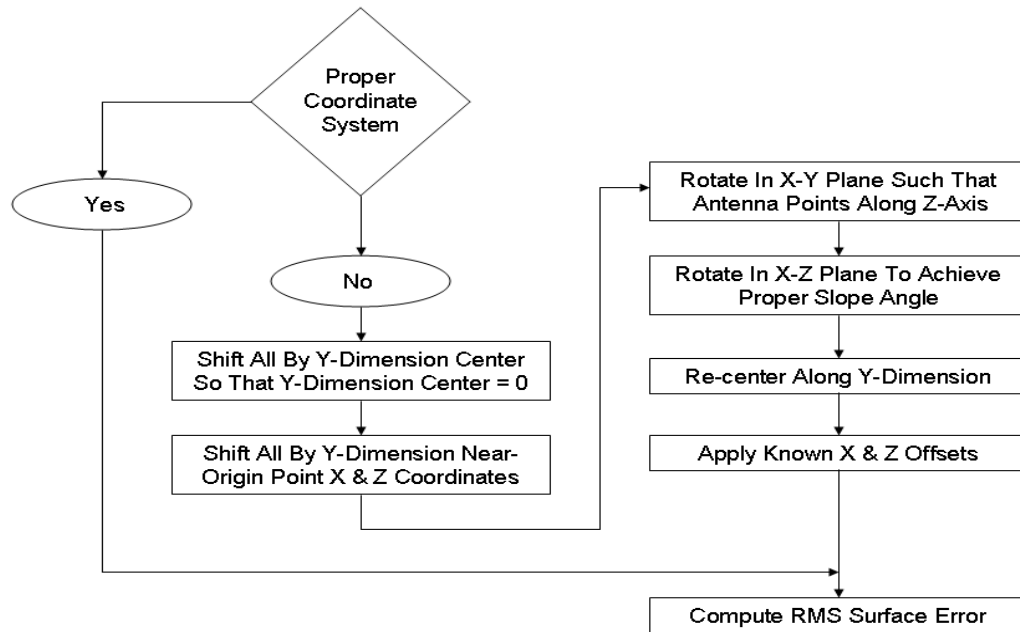


Figure 16: Coordinate Transformation Block Diagram

As shown in the block diagram in Figure 16, the final step is to compute the RMS surface error. The surface error is computed via methods described in Section 2.3 of this thesis. The ideal surface is computed using the known focal length and the measured  $x$  and  $y$  coordinates. The error is computed in the axial direction, which is along  $z$ -axis. The reason for the transformation of the data points is to be able to properly determine the ideal paraboloid, from Equation 20.

$$z = \frac{1}{4f}(x^2 + y^2) \quad (20)$$

In Equation 20, the additional terms used are defined as follows:

- $x, y, z$  are the Cartesian coordinates along the paraboloid
- $f$  is the focal length of the paraboloid

## **CHAPTER IV**

### **RESULTS**

Chapter Four will present results of the tests performed on the offset inflatable aperture antenna for the different pressurization levels. Section 4.1 will provide detailed directivity and beam pattern results from the Planar Near-Field RF scans. The raw and transformed photogrammetry data will be presented and compared with ideal paraboloidal data in Section 4.2. The RMS surface error will also be calculated here. Finally, comparisons will be made between the surface error loss exhibited in the Planar Near-Field RF scans on the antenna and what is predicted from the Ruze Equation via the RMS surface error.

#### **4.1 RF Performance**

Planar Near-Field RF antenna testing results will be presented in this section. The antenna was tested at 8.4 GHz with a known efficiency of 0.68, based on the loss due to the 11 dB taper from the antenna feed. Based on the diameter of the inflatable aperture antenna and the known efficiency accounted for, the ideal antenna gain is 26.753 dBi.

Plots will be shown with co-polarization and cross-polarization results in the azimuth and elevation dimensions. Co-polarization results will be shown in a solid line while cross-polarization results will be shown in a dashed line. All graphics have been normalized to 0 dBi from the directivity value at that pressurization.

Pressurization Set at 0.000 Inches H<sub>2</sub>O

The inflatable aperture antenna was inflated with a pressurization of ambient air of 0.000 inches H<sub>2</sub>O. For this case, this meant that the antenna was un-inflated. Due to the effect of gravity, the aperture was not held in the proper direction. The plots of the far-field beam patterns in the azimuth direction are shown in Figure 17, while the far-field beam patterns in the elevation direction are shown in Figure 18.

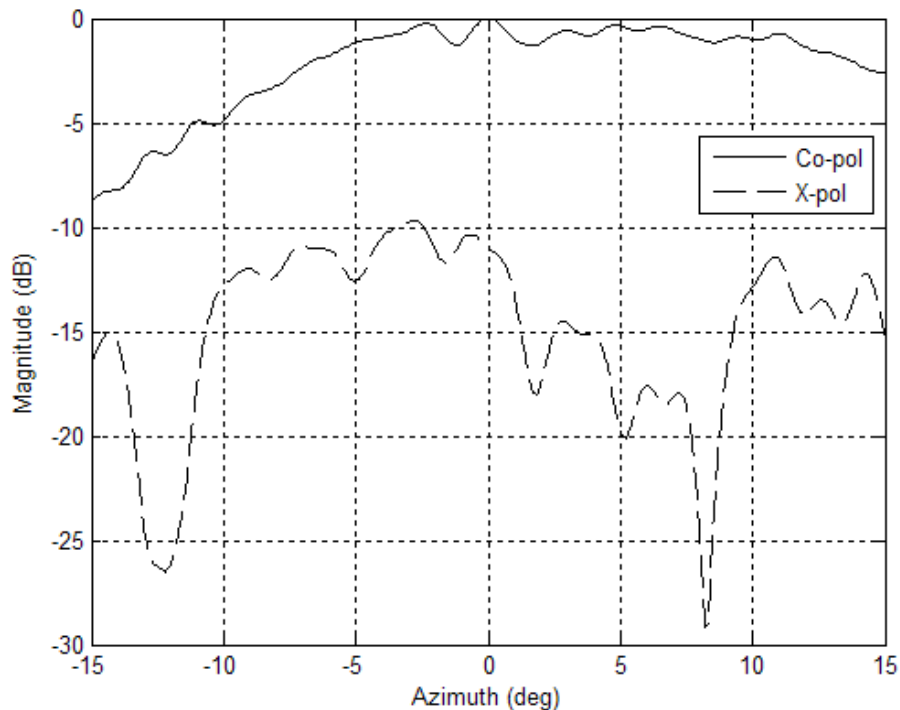


Figure 17: Azimuth Far-Field Patterns, 0.000 inch H<sub>2</sub>O Pressurization

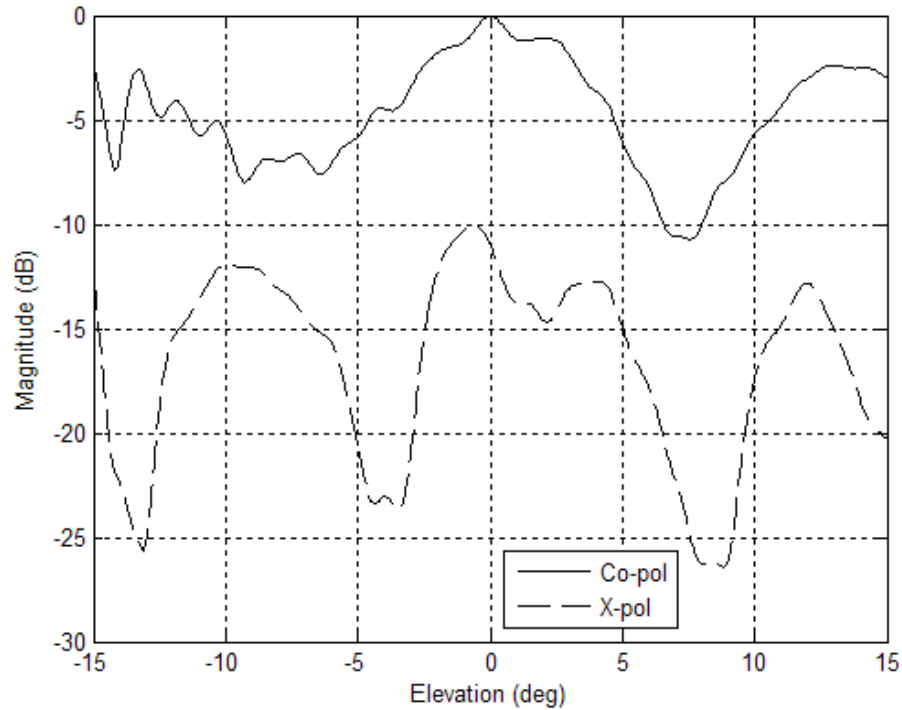


Figure 18: Elevation Far-Field Patterns, 0.000 inch H<sub>2</sub>O Pressurization

The measured directivity of the inflatable aperture antenna was 14.424 dBi. Therefore, the surface loss of the antenna was -12.329 dB. Note that in Figure 17, there are no distinguishable nulls present for the co-polarization in the azimuth dimension. In Figure 18, there are nulls present at around  $\pm 7^\circ$  with a magnitude that is roughly 7 to 11 dB down below the peak directivity for the co-polarization in the elevation dimension, respectively.

*Pressurization Set at 0.030 Inches H<sub>2</sub>O*

The inflatable aperture antenna was inflated with a pressurization of ambient air of 0.030 inches H<sub>2</sub>O. The plots of the far-field beam patterns in the azimuth direction are

shown in Figure 19, while the far-field beam patterns in the elevation direction are shown in Figure 20.

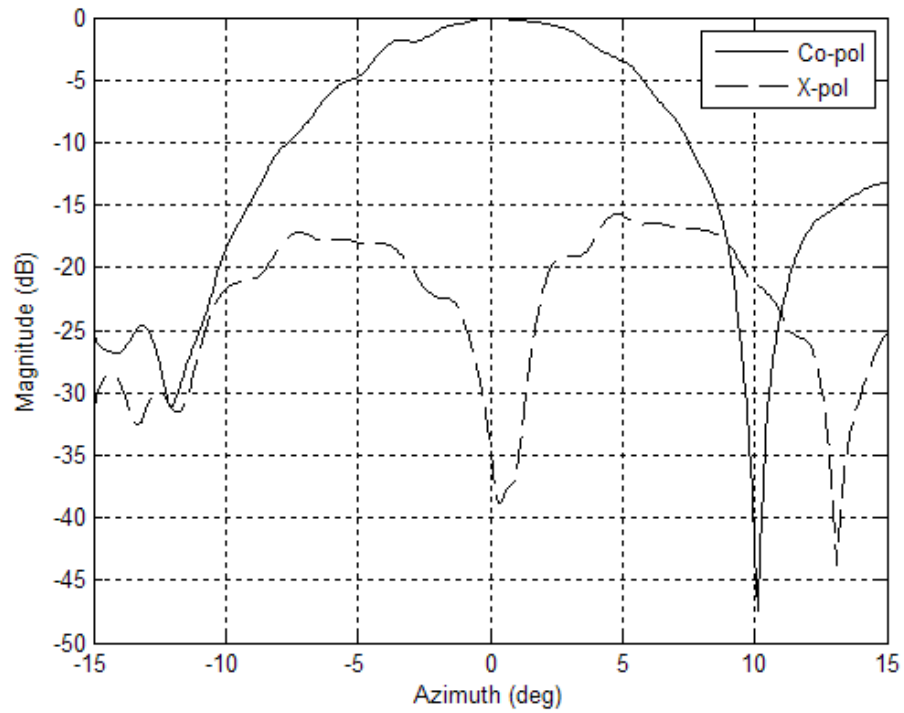


Figure 19: Azimuth Far-Field Patterns, 0.030 inch H<sub>2</sub>O Pressurization

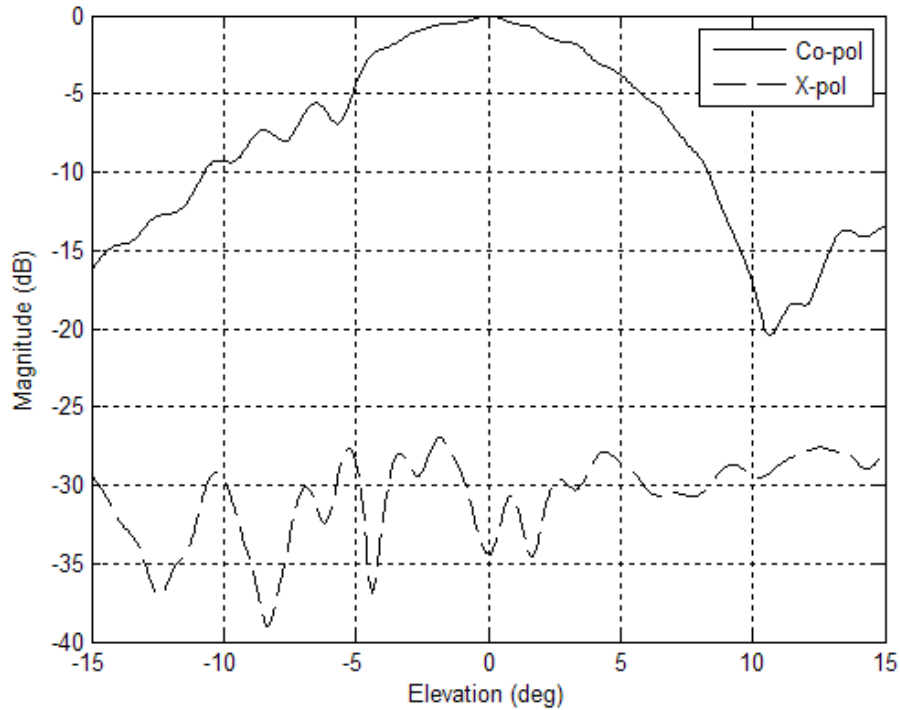


Figure 20: Elevation Far-Field Patterns, 0.030 inch H<sub>2</sub>O Pressurization

The measured directivity of the inflatable aperture antenna was 23.141 dBi. Therefore, the surface loss of the antenna was  $-3.612$  dB. In Figure 19, there are distinguishable nulls present for the co-polarization at roughly  $10^\circ$  and  $-12^\circ$  in the azimuth dimension that are roughly 47 and 31 dB down below the peak directivity, respectively. In Figure 20, there is a null present at around  $11^\circ$  with a magnitude that is roughly 20 dB down below the peak directivity for the co-polarization in the elevation dimension.

Pressurization Set at 0.040 Inches H<sub>2</sub>O

The inflatable aperture antenna was inflated with a pressurization of ambient air of 0.040 inches H<sub>2</sub>O. The plots of the far-field beam patterns in the azimuth direction are

shown in Figure 21, while the far-field beam patterns in the elevation direction are shown in Figure 22.

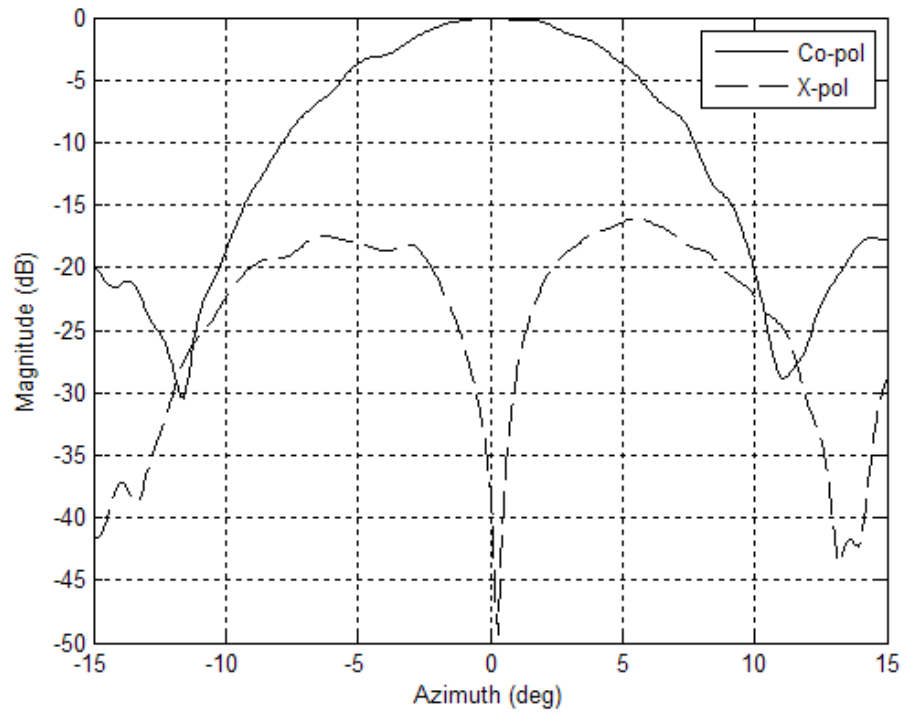


Figure 21: Azimuth Far-Field Patterns, 0.040 inch H<sub>2</sub>O Pressurization

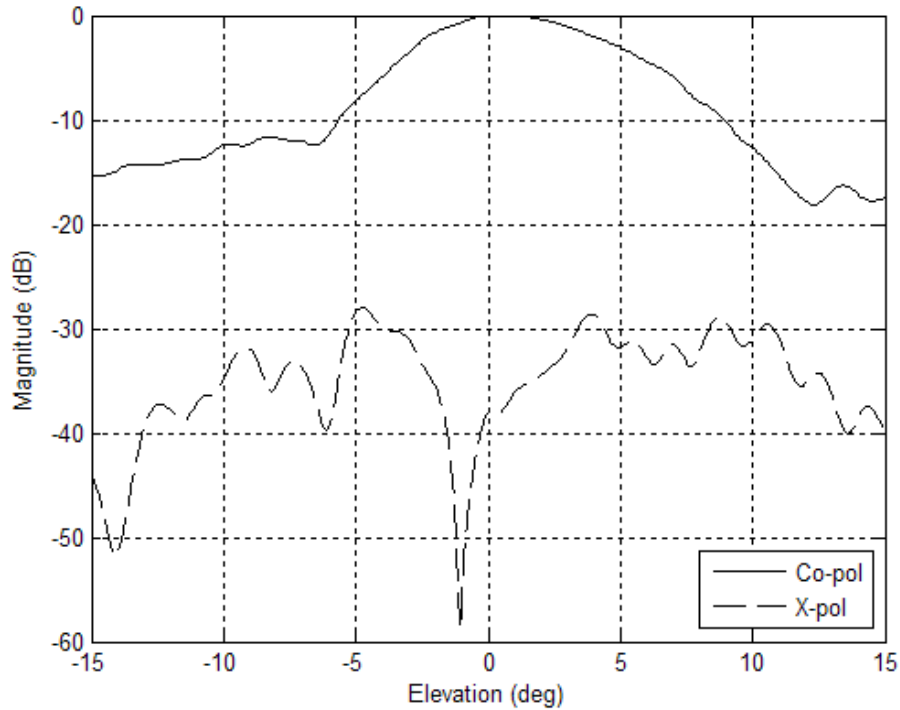


Figure 22: Elevation Far-Field Patterns, 0.040 inch H<sub>2</sub>O Pressurization

The measured directivity of the inflatable aperture antenna was 24.371 dBi. Therefore, the surface loss of the antenna was  $-2.382$  dB. Note that in Figure 21, there are distinguishable nulls present for the co-polarization at roughly  $11^\circ$  and  $-11.5^\circ$  in the azimuth dimension that are roughly 28 and 30 dB down below the peak directivity, respectively. In Figure 22, there are nulls present at around  $12.5^\circ$  and  $-6^\circ$  with magnitudes that are roughly 18 and 12 dB down below the peak directivity for the co-polarization in the elevation dimension, respectively.

Pressurization Set at 0.050 Inches H<sub>2</sub>O

The inflatable aperture antenna was inflated with a pressurization of ambient air of 0.050 inches H<sub>2</sub>O. The plots of the far-field beam patterns in the azimuth direction are

shown in Figure 23, while the far-field beam patterns in the elevation direction are shown in Figure 24.

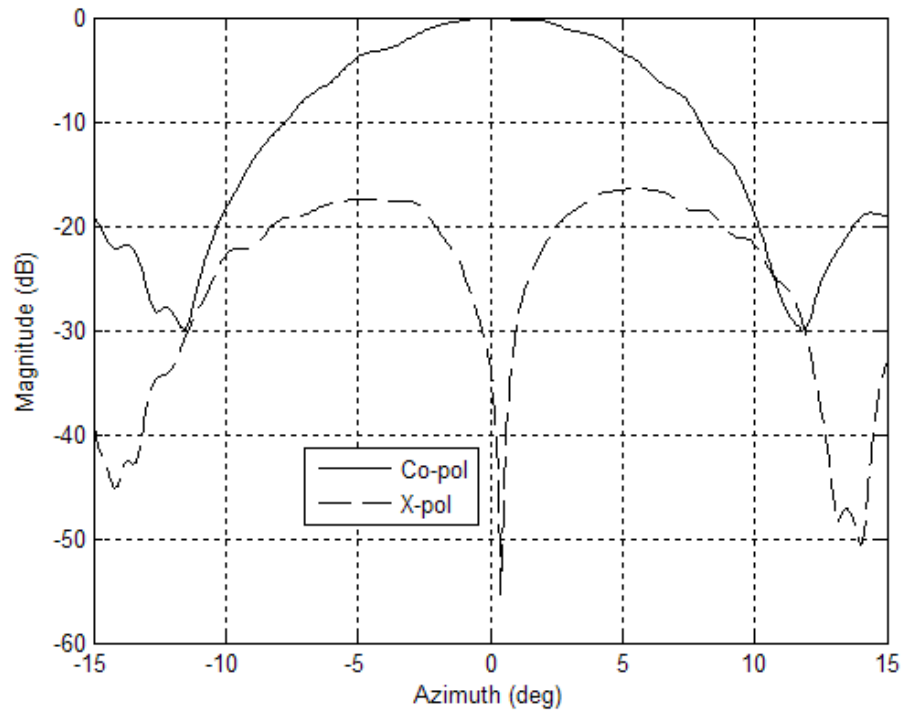


Figure 23: Azimuth Far-Field Patterns, 0.050 inch H<sub>2</sub>O Pressurization

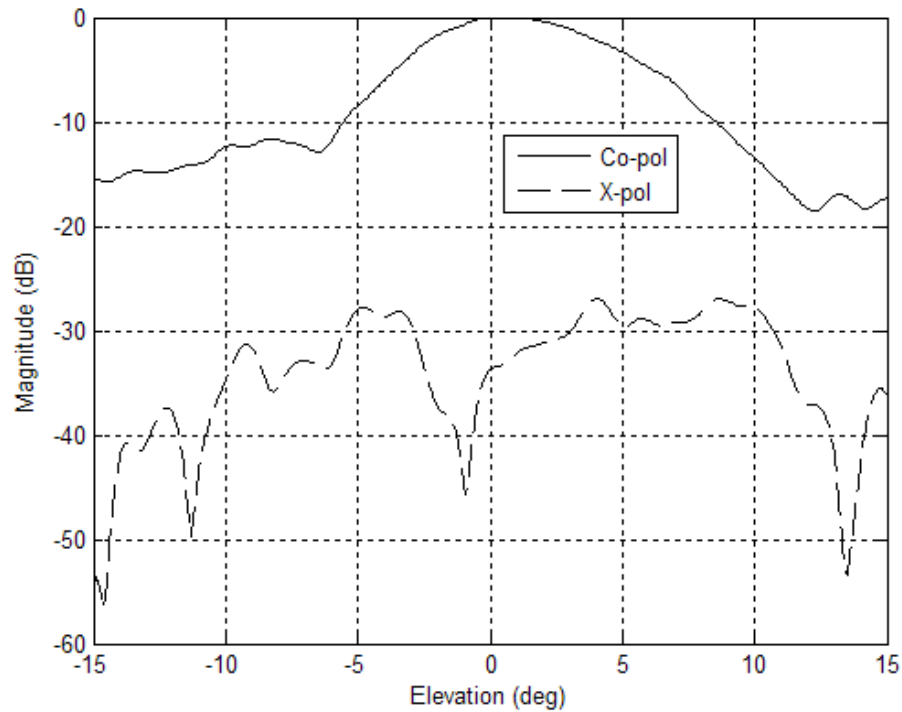


Figure 24: Elevation Far-Field Patterns, 0.050 inch H<sub>2</sub>O Pressurization

The measured directivity of the inflatable aperture antenna was 24.521 dBi. Therefore, the surface loss of the antenna was  $-2.232$  dB. Note that in Figure 23, there are distinguishable nulls present for the co-polarization at roughly  $\pm 12^\circ$  in the azimuth dimension that are roughly 30 dB down below the peak directivity. In Figure 24, there are nulls present at around  $12.5^\circ$  and  $-6^\circ$  with magnitudes that are roughly 18 and 13 dB down below the peak directivity for the co-polarization in the elevation dimension, respectively.

#### Pressurization Set at 0.060 Inches H<sub>2</sub>O

The inflatable aperture antenna was inflated with a pressurization of ambient air of 0.060 inches H<sub>2</sub>O. The plots of the far-field beam patterns in the azimuth direction are

shown in Figure 25, while the far-field beam patterns in the elevation direction are shown in Figure 26.

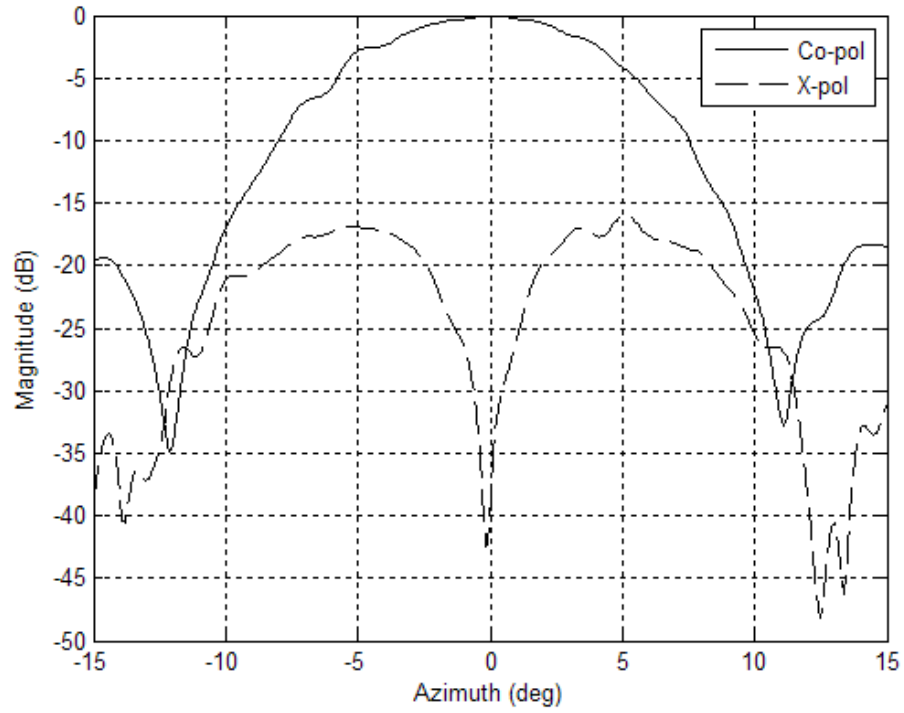


Figure 25: Azimuth Far-Field Patterns, 0.060 inch H<sub>2</sub>O Pressurization

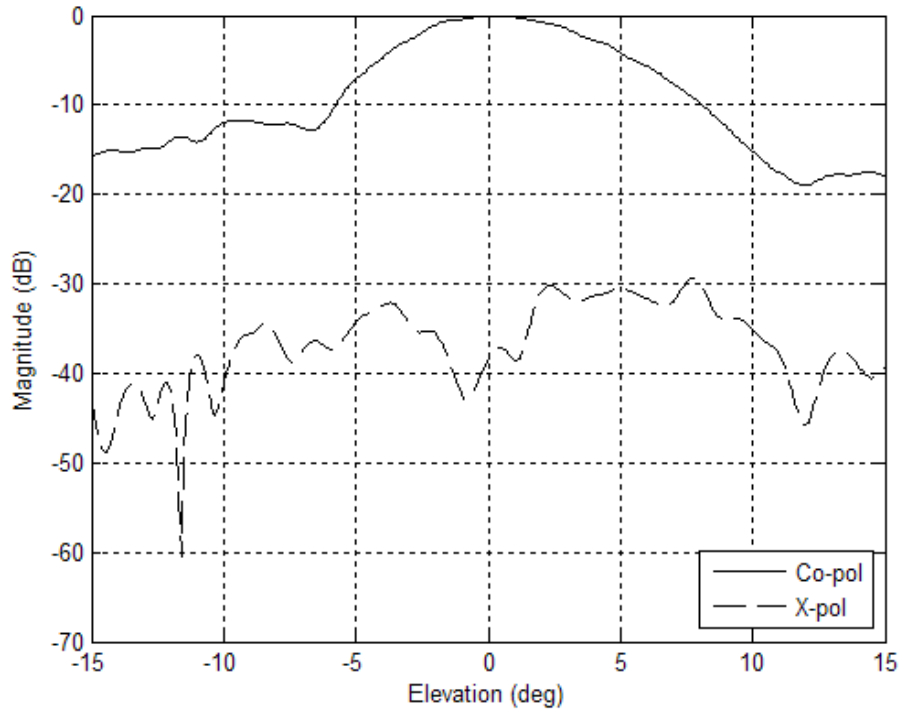


Figure 26: Elevation Far-Field Patterns, 0.060 inch H<sub>2</sub>O Pressurization

The measured directivity of the inflatable aperture antenna was 24.473 dBi. Therefore, the surface loss of the antenna was  $-2.280$  dB. Note that in Figure 25, there are distinguishable nulls present for the co-polarization at roughly  $11.5^\circ$  and  $-12^\circ$  in the azimuth dimension that are roughly 33 and 35 dB down below the peak directivity, respectively. In Figure 26, there are nulls present at around  $12.5^\circ$  and  $-6^\circ$  with magnitudes that are roughly 19 and 13 dB down below the peak directivity for the co-polarization in the elevation dimension, respectively.

Pressurization Set at 0.070 Inches H<sub>2</sub>O

The inflatable aperture antenna was inflated with a pressurization of ambient air of 0.070 inches H<sub>2</sub>O. The plots of the far-field beam patterns in the azimuth direction are

shown in Figure 27, while the far-field beam patterns in the elevation direction are shown in Figure 28.

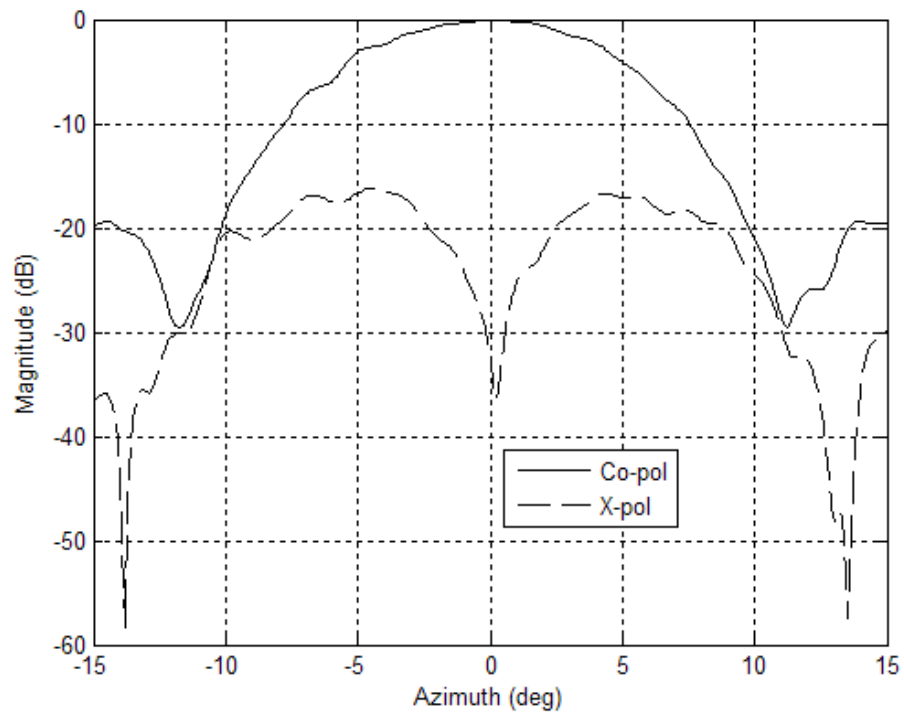


Figure 27: Azimuth Far-Field Patterns, 0.070 inch H<sub>2</sub>O Pressurization

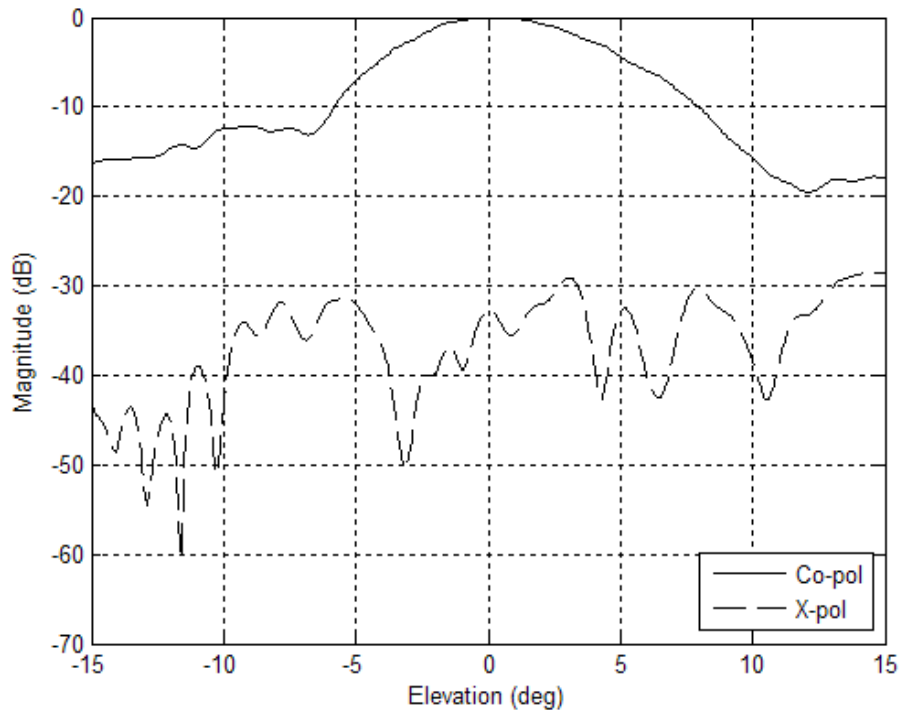


Figure 28: Elevation Far-Field Patterns, 0.070 inch H<sub>2</sub>O Pressurization

The measured directivity of the inflatable aperture antenna was 24.453 dBi. Therefore, the surface loss of the antenna was  $-2.300$  dB. Note that in Figure 27, there are distinguishable nulls present for the co-polarization at roughly  $11.5^\circ$  and  $-12^\circ$  in the azimuth dimension that are roughly 30 dB down below the peak directivity. In Figure 28, there are nulls present at around  $12^\circ$  and  $-6.5^\circ$  with magnitudes that are roughly 20 and 13 dB down below the peak directivity for the co-polarization in the elevation dimension, respectively.

#### RF Performance Summary

TABLE III provides a summary of the directivity and the surface loss that is experienced by the 0.3 meter offset inflatable aperture antenna for the six different

pressurizations that the antenna was tested with. Note that the pressurization that produced the largest directivity was 0.050 inch H<sub>2</sub>O.

**TABLE III:** RF Pressurization Performance Comparison

<b>Pressurization</b>	<b>RF Directivity</b>	<b>Surface Loss</b>
0.000 inch H <sub>2</sub> O	14.424 dBi	-12.329 dB
0.030 inch H <sub>2</sub> O	23.141 dBi	-3.612 dB
0.040 inch H <sub>2</sub> O	24.371 dBi	-2.382 dB
0.050 inch H <sub>2</sub> O	24.521 dBi	-2.232 dB
0.060 inch H <sub>2</sub> O	24.473 dBi	-2.280 dB
0.070 inch H <sub>2</sub> O	24.453 dBi	-2.300 dB

## 4.2 RMS Performance

Photogrammetry antenna testing results will be presented in this section. The antenna was scanned at spacing intervals in the x and y dimension of 0.1 inch. This spatial separation between is well below the Nyquist minimum of 0.703 inches. Plots will be shown of the raw photogrammetry data, along with a plot containing the transformed photogrammetry data with the ideal paraboloid shown in the X-Z plane, in which the transformed data is darker than the ideal paraboloid.

### Pressurization Set at 0.000 Inches H<sub>2</sub>O

The inflatable aperture antenna was inflated with a pressurization of ambient air of 0.000 inches H<sub>2</sub>O, meaning that the antenna was un-inflated. Due to the effect of gravity, the aperture was not held in the proper direction. A plot of the raw

photogrammetry data is shown in Figure 29. Figure 30 shows the transformed photogrammetry data and the ideal paraboloid.

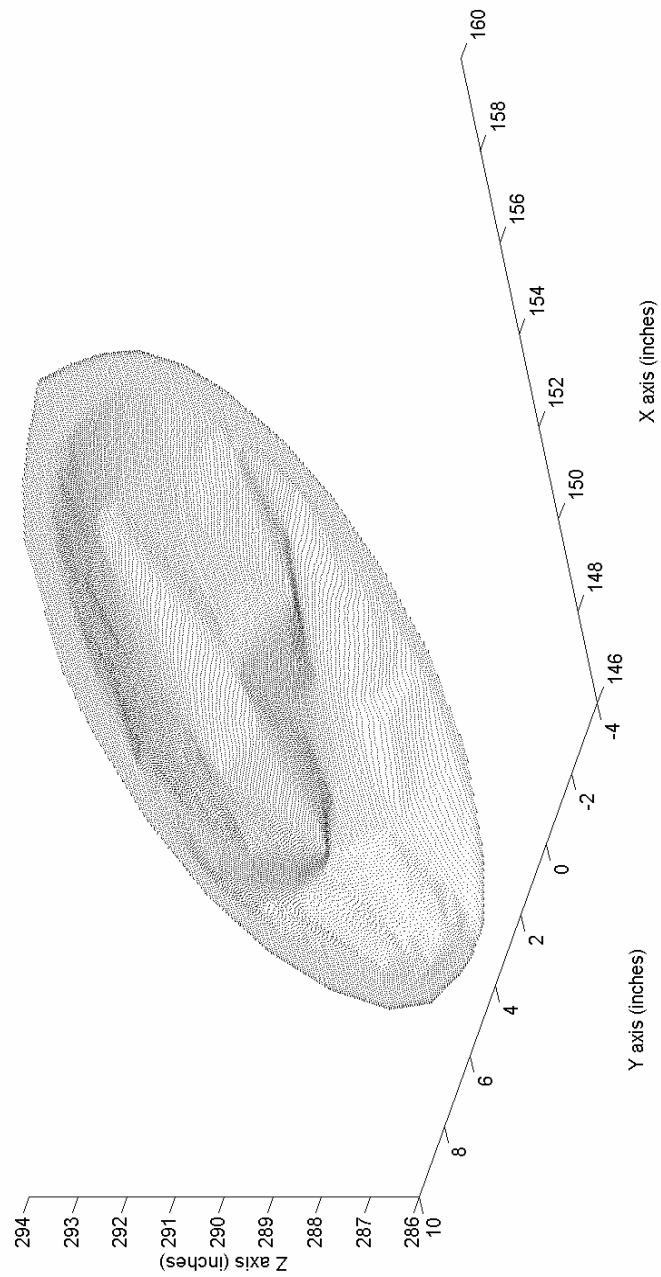


Figure 29: Raw Photogrammetry Data, 0.000 inch H<sub>2</sub>O Pressurization

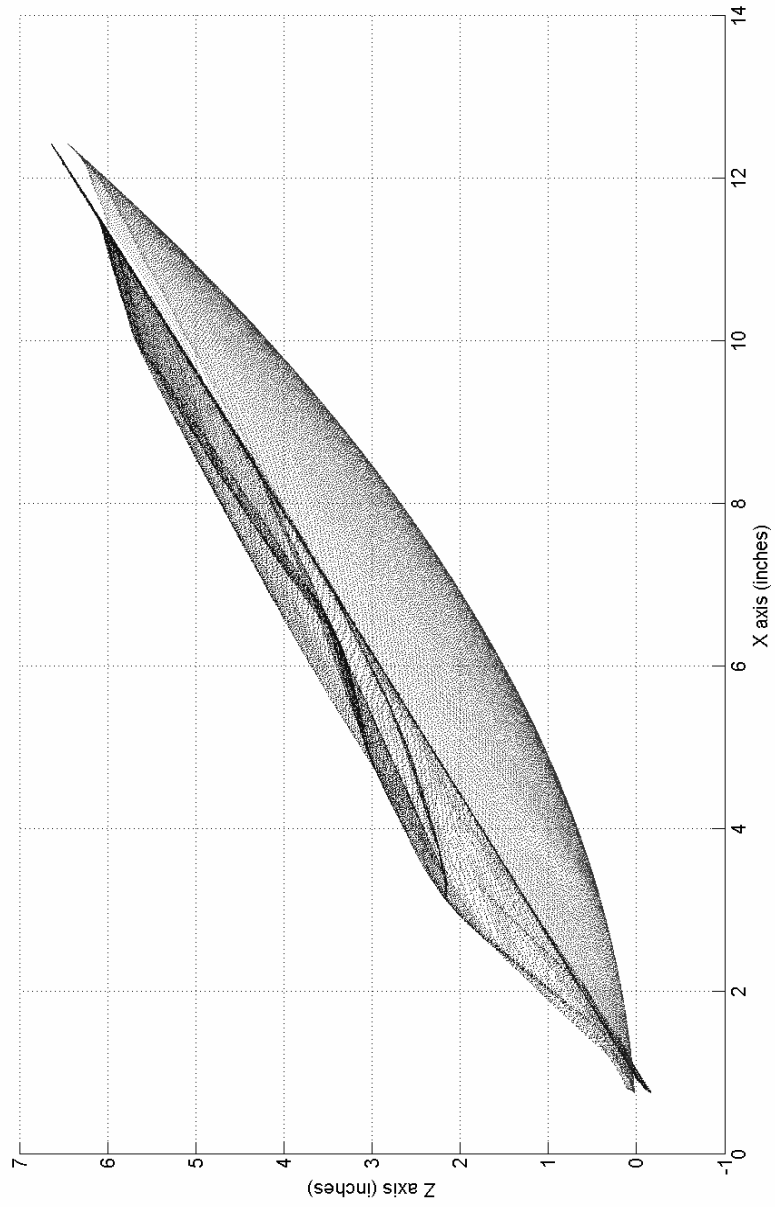


Figure 30: Transformed & Ideal Paraboloid, 0.000 inch H<sub>2</sub>O Pressurization

The RMS surface error that was calculated was 1.2036 inches. Therefore, according to the Ruze Equation, the surface loss should be -402.015 dB. Figure 29 shows clearly defined wrinkles on the antenna surface. Figure 30 shows how the antenna was no longer maintaining its shape as gravity had caused the antenna to invert. Note also that the Hencky curve can still be observed near the antenna edges.

*Pressurization Set at 0.030 Inches H<sub>2</sub>O*

The inflatable aperture antenna was inflated with a pressurization of ambient air of 0.030 inches H<sub>2</sub>O. A plot of the raw photogrammetry data is shown in Figure 31. Figure 32 shows the transformed photogrammetry data and the ideal paraboloid.

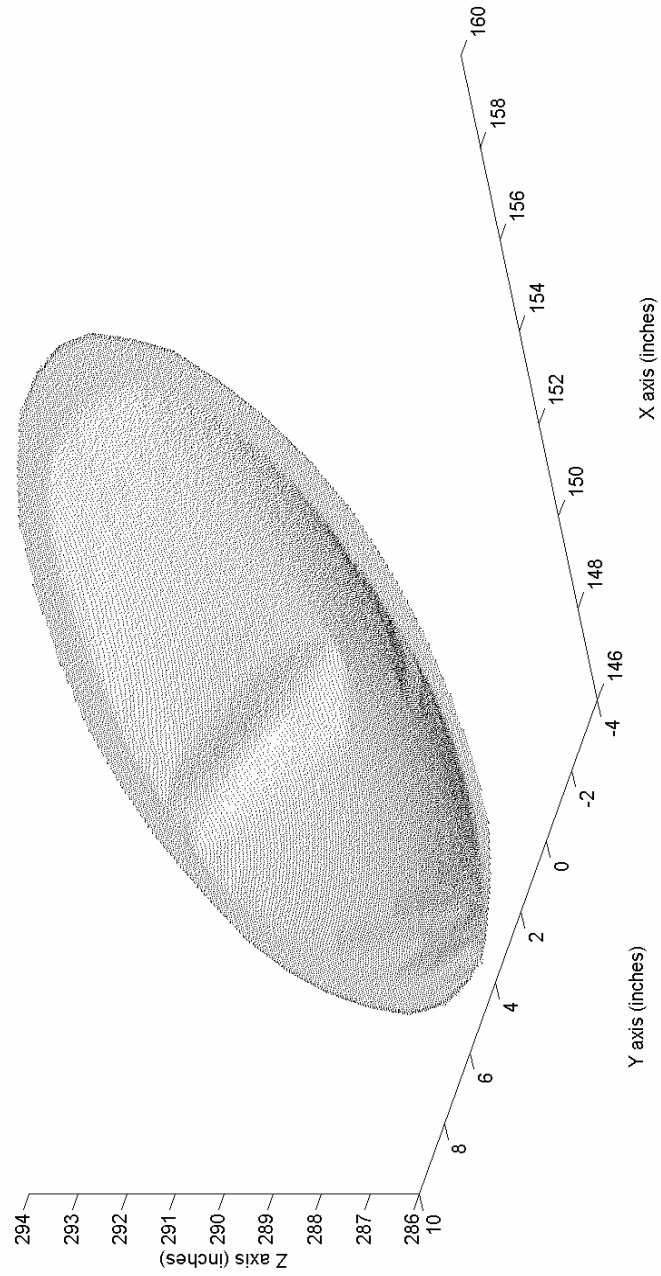


Figure 31: Raw Photogrammetry Data, 0.030 inch H<sub>2</sub>O Pressurization

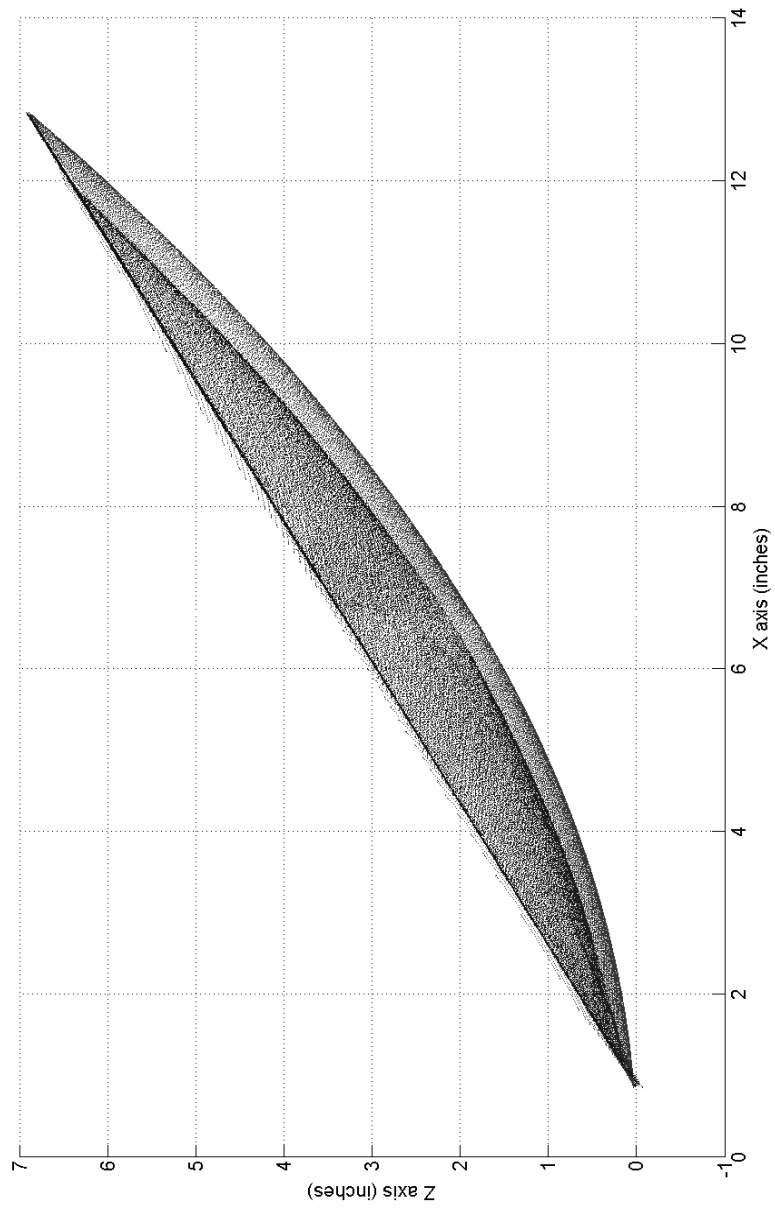


Figure 32: Transformed & Ideal Paraboloid, 0.030 inch H<sub>2</sub>O Pressurization

The RMS surface error that was calculated was 0.3407 inches. Therefore, according to the Ruze Equation, the surface loss should be -32.212 dB. Figure 31 shows one large wrinkle and several smaller wrinkles on the antenna surface. Figure 32 shows how the antenna was affected by the inflation process involving the creation of the Hencky curve near the antenna edges.

*Pressurization Set at 0.040 Inches H<sub>2</sub>O*

The inflatable aperture antenna was inflated with a pressurization of ambient air of 0.040 inches H<sub>2</sub>O. A plot of the raw photogrammetry data is shown in Figure 33. Figure 34 shows the transformed photogrammetry data and the ideal paraboloid.

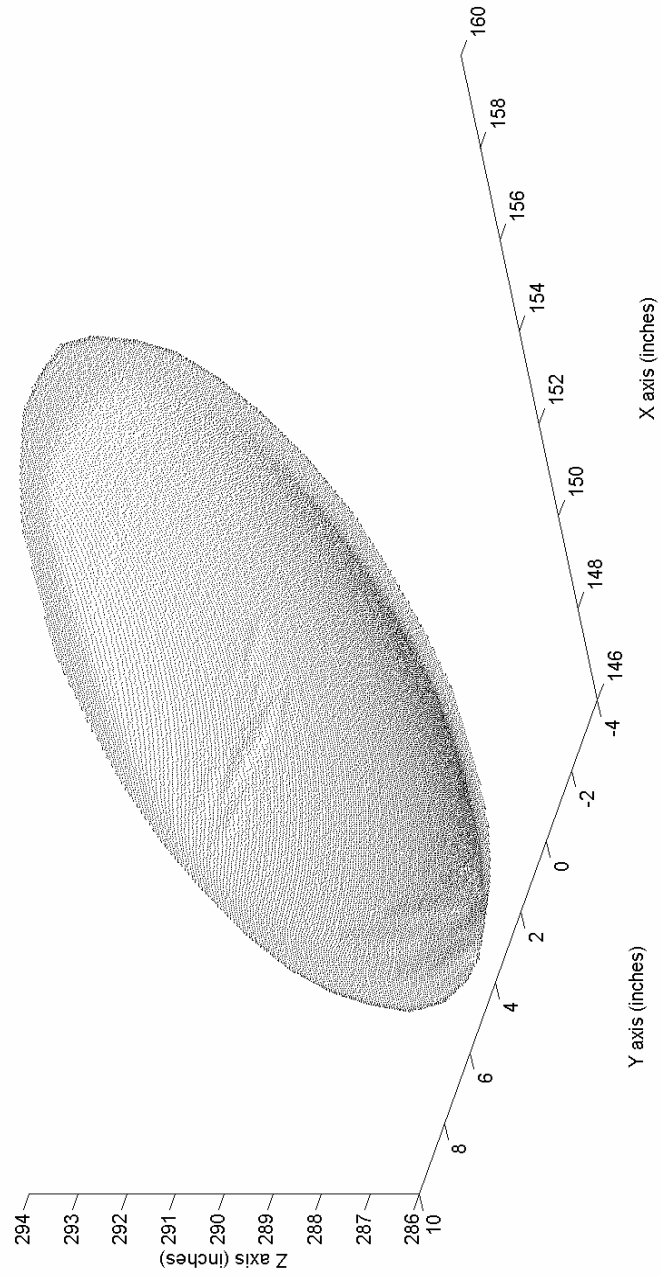


Figure 33: Raw Photogrammetry Data, 0.040 inch H<sub>2</sub>O Pressurization

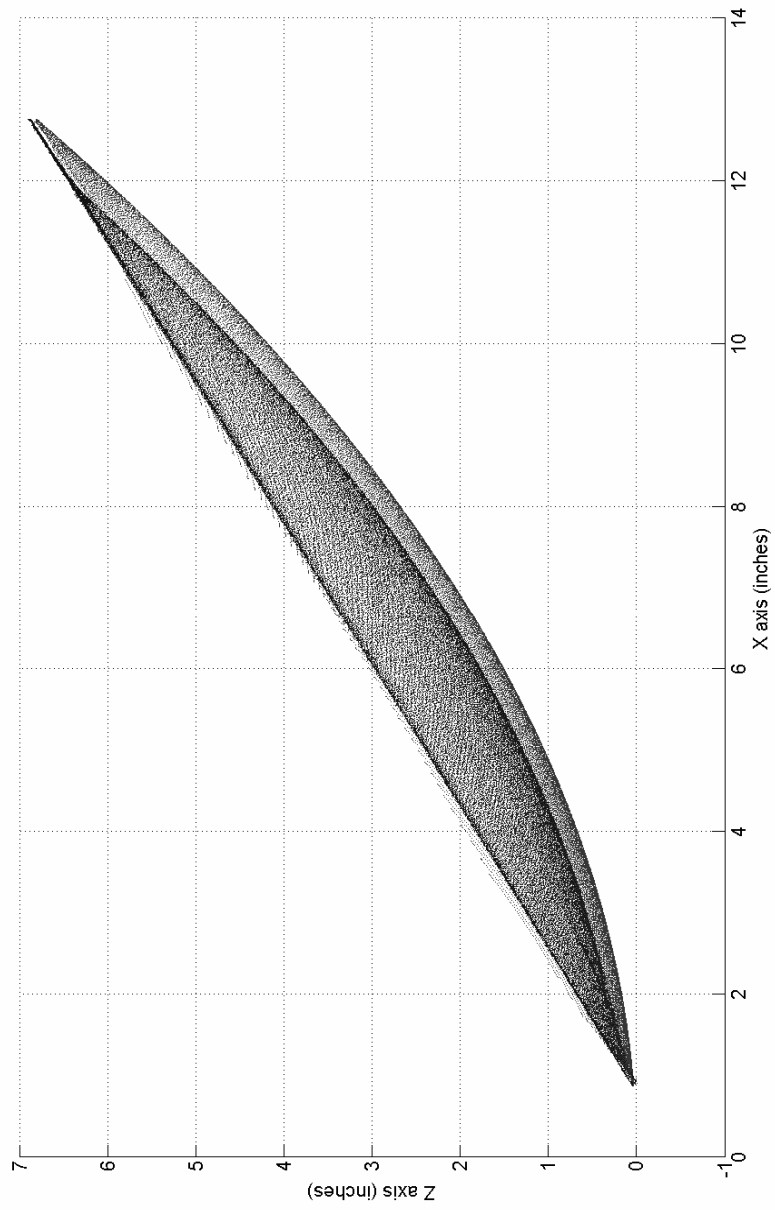


Figure 34: Transformed & Ideal Paraboloid, 0.040 inch H<sub>2</sub>O Pressurization

The RMS surface error that was calculated was 0.2620 inches. Therefore, according to the Ruze Equation, the surface loss should be -19.049 dB. Figure 33 shows several smaller wrinkles on the antenna surface than at lower pressurizations. Figure 34 shows how the antenna was affected by the inflation process involving the creation of the Hencky curve near the antenna edges. Note that as the pressurization increases, the amount of the antenna surface affected by the Hencky curve decreases.

*Pressurization Set at 0.050 Inches H<sub>2</sub>O*

The inflatable aperture antenna was inflated with a pressurization of ambient air of 0.050 inches H<sub>2</sub>O. A plot of the raw photogrammetry data is shown in Figure 35. Figure 36 shows the transformed photogrammetry data and the ideal paraboloid.

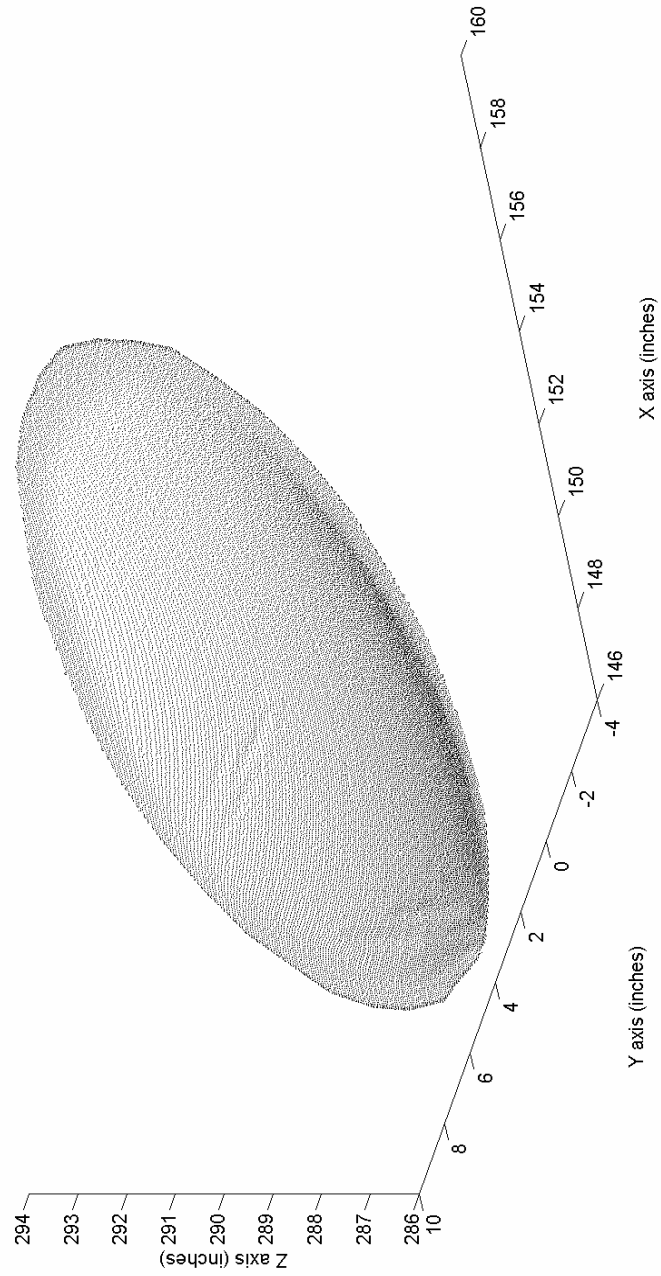


Figure 35: Raw Photogrammetry Data, 0.050 inch H<sub>2</sub>O Pressurization

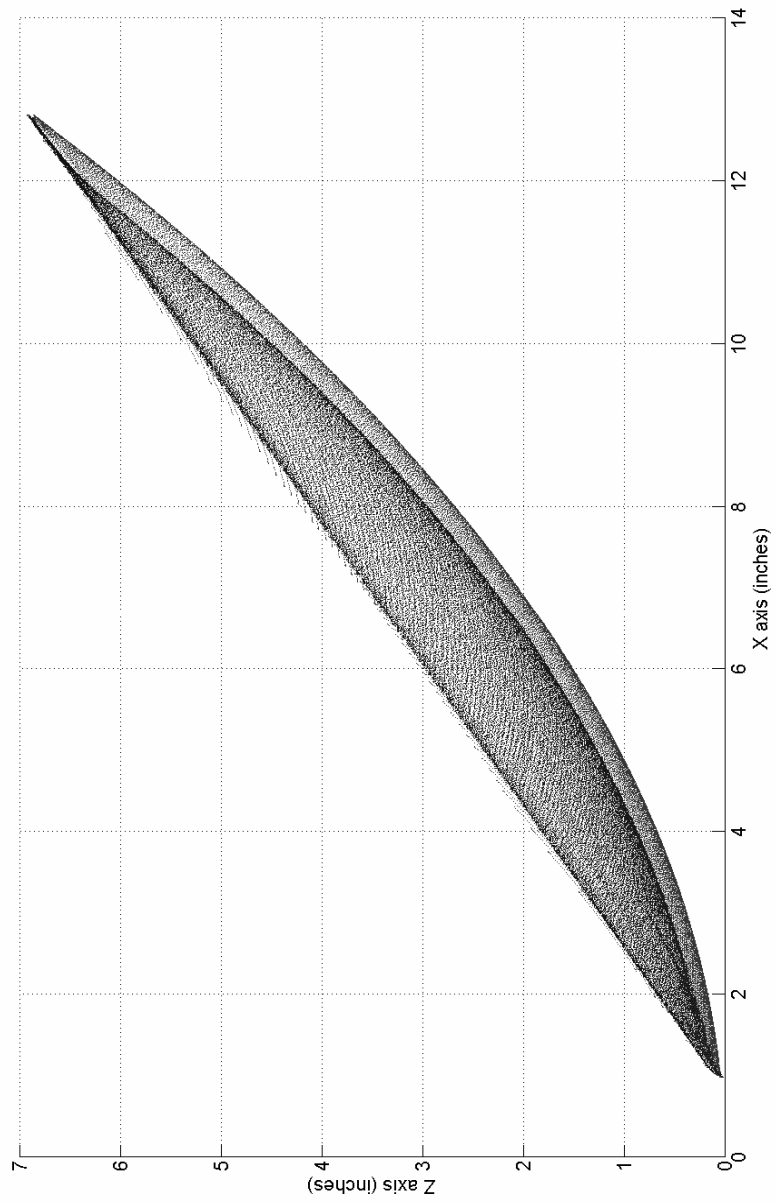


Figure 36: Transformed & Ideal Paraboloid, 0.050 inch H<sub>2</sub>O Pressurization

The RMS surface error that was calculated was 0.2334 inches. Therefore, according to the Ruze Equation, the surface loss should be -15.117 dB. Figure 35 shows several smaller wrinkles on the antenna surface than at lower pressurizations. Figure 36 shows how the antenna was affected by the inflation process involving the creation of the Hencky curve near the antenna edges. Note that as the pressurization increases, the amount of the antenna surface affected by the Hencky curve decreases.

*Pressurization Set at 0.060 Inches H<sub>2</sub>O*

The inflatable aperture antenna was inflated with a pressurization of ambient air of 0.060 inches H<sub>2</sub>O. A plot of the raw photogrammetry data is shown in Figure 37. Figure 38 shows the transformed photogrammetry data and the ideal paraboloid.

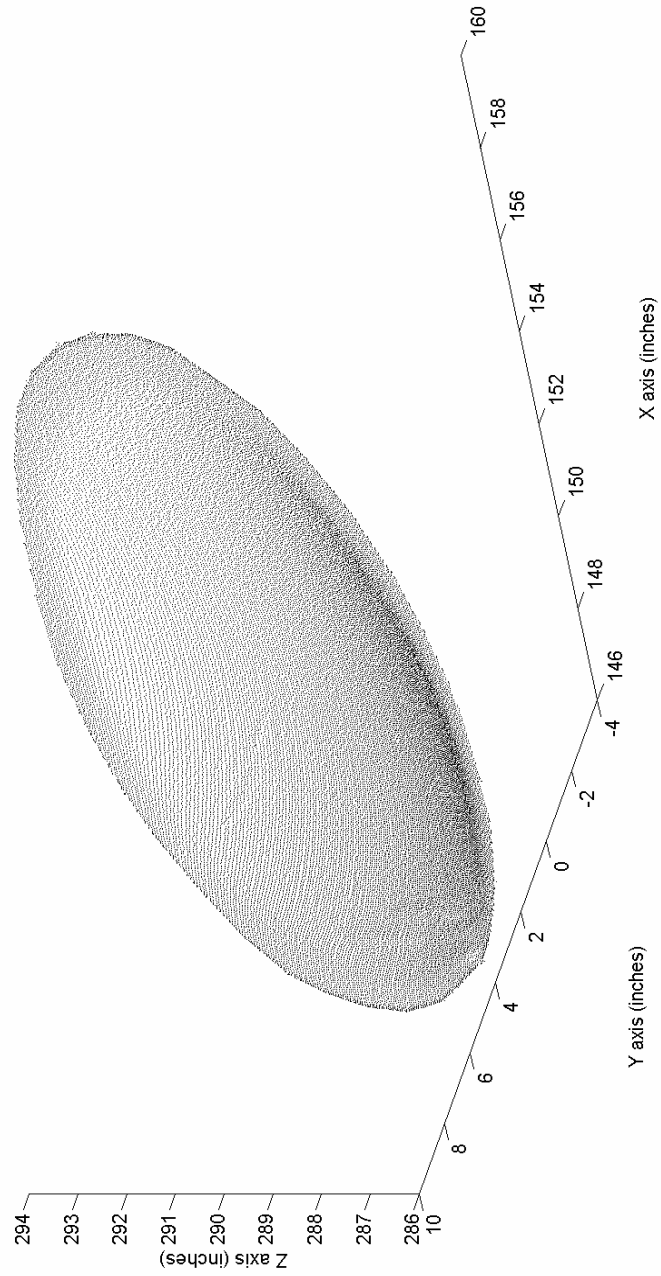


Figure 37: Raw Photogrammetry Data, 0.060 inch H<sub>2</sub>O Pressurization

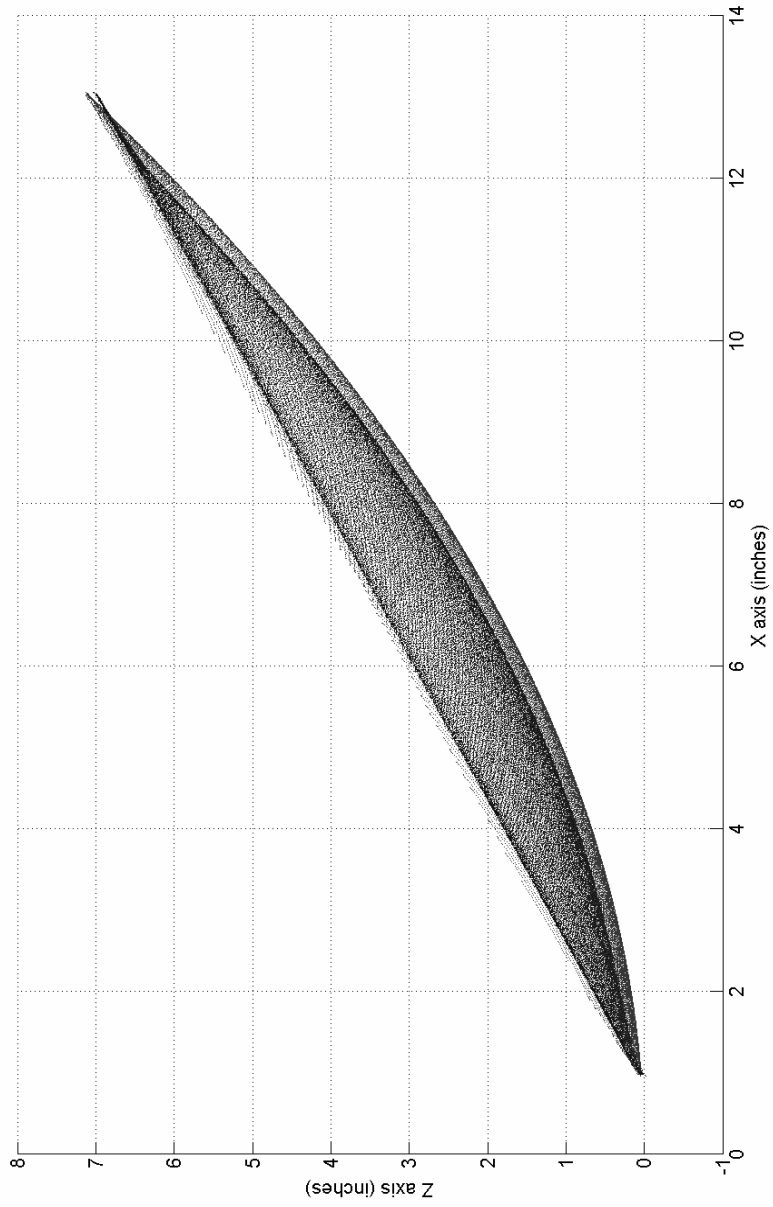


Figure 38: Transformed & Ideal Paraboloid, 0.060 inch H<sub>2</sub>O Pressurization

The RMS surface error that was calculated was 0.1885 inches. Therefore, according to the Ruze Equation, the surface loss should be -9.861 dB. Figure 37 shows a few very small wrinkles on the antenna surface near the region of inflation control for the aperture. Figure 38 shows how the antenna was affected by the inflation process involving the creation of the Hencky curve near the antenna edges. Note that at this pressurization, there is less of an effect from the Hencky curve than for prior pressurizations.

*Pressurization Set at 0.070 Inches H<sub>2</sub>O*

The inflatable aperture antenna was inflated with a pressurization of ambient air of 0.070 inches H<sub>2</sub>O. A plot of the raw photogrammetry data is shown in Figure 39. Figure 40 shows the transformed photogrammetry data and the ideal paraboloid.

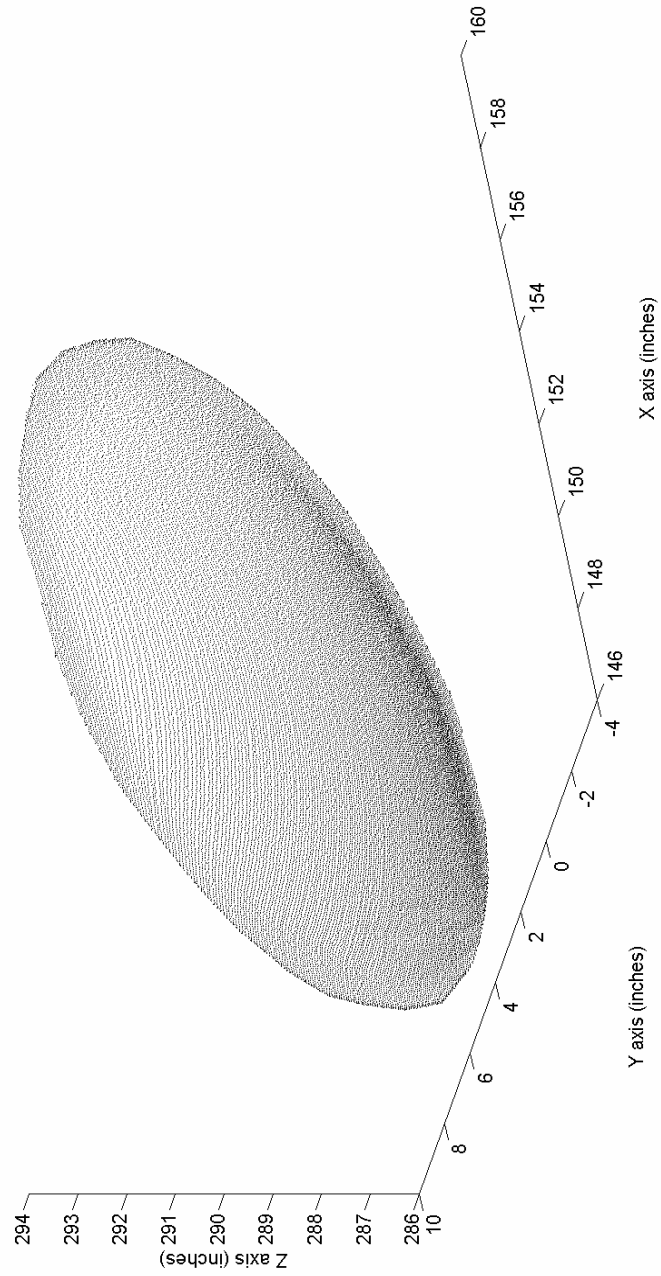


Figure 39: Raw Photogrammetry Data, 0.070 inch H<sub>2</sub>O Pressurization

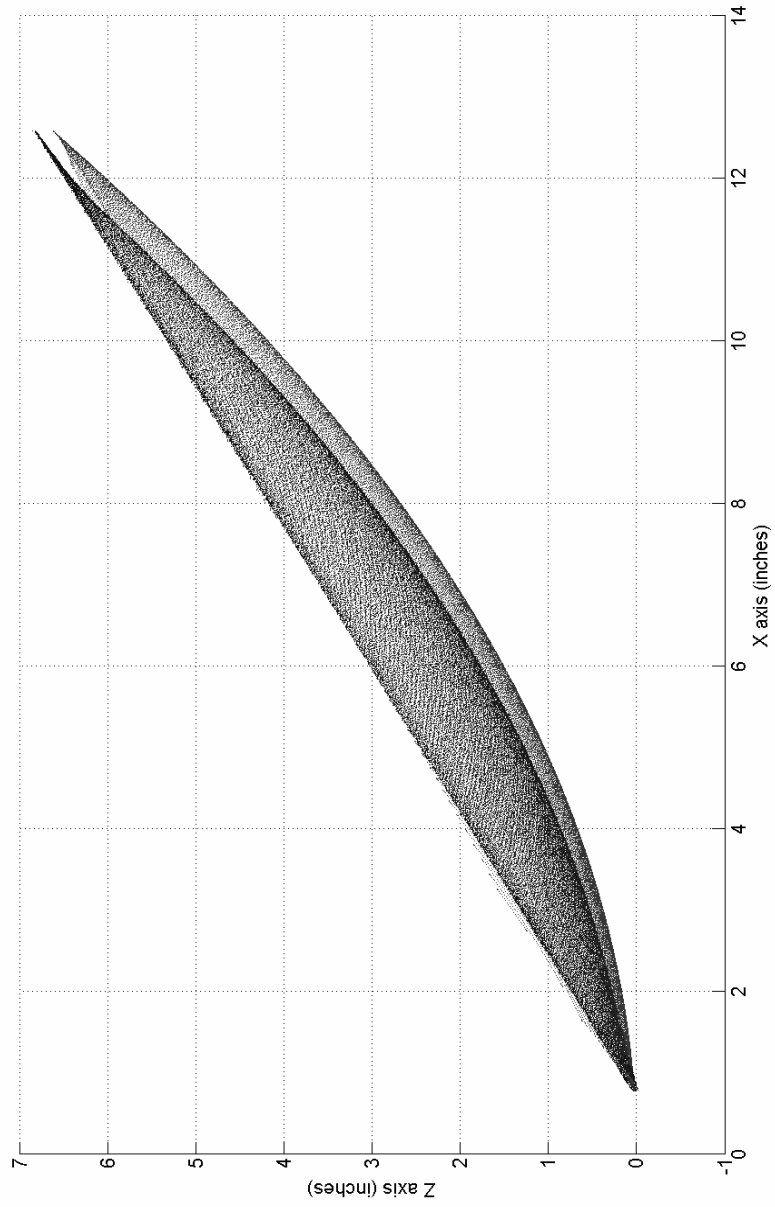


Figure 40: Transformed & Ideal Paraboloid, 0.070 inch H<sub>2</sub>O Pressurization

The RMS surface error that was calculated was 0.2649 inches. Therefore, according to the Ruze Equation, the surface loss should be -19.473 dB. Figure 39 shows a few very small wrinkles on the antenna surface near the region of inflation control for the aperture. Figure 40 shows how the antenna was affected by the inflation process involving the creation of the Hencky curve near the antenna edges. Note that at this pressurization, the antenna is starting to become over-inflated and can be seen in the comparison between the ideal and measured paraboloids.

*RMS Performance Summary*

TABLE IV provides a summary of the RMS surface error and the Ruze Equation predicted surface loss for the 0.3 meter offset inflatable aperture antenna for the six different pressurizations that the antenna was tested with. Note that the pressurization that produced the smallest RMS surface error was 0.060 inch H<sub>2</sub>O. This is not the same pressurization that produced the largest directivity from the RF pressurization performance analysis.

**TABLE IV: RMS Pressurization Performance Comparison**

<b>Pressurization</b>	<b>RMS Surface Error</b>	<b>Ruze-Derived Surface Loss</b>
0.000 inch H <sub>2</sub> O	1.2036 Inch	-402.015 dB
0.030 inch H <sub>2</sub> O	0.3407 Inch	-32.212 dB
0.040 inch H <sub>2</sub> O	0.2620 Inch	-19.049 dB
0.050 inch H <sub>2</sub> O	0.2334 Inch	-15.117 dB
0.060 inch H <sub>2</sub> O	0.1885 Inch	-9.861 dB
0.070 inch H <sub>2</sub> O	0.2649 Inch	-19.473 dB

### 4.3 Ruze Equation Performance

The previous two sections have provided information about the directivity and beam pattern measurements taken from the Planar Near-Field Antenna Test Facility at NASA Glenn Research Center and photogrammetry-derived Ruze Equation predictions for the directivity degradation due to surface errors. Those results are tabulated below in Table V per the various pressurization levels. The difference between the RF performance and the Ruze-derived performance is also calculated; where a positive number means that the Ruze Equation over-states the surface loss.

**TABLE V: RF & Ruze Equation Performance Comparisons**

<b>Pressurization</b>	<b>RF Directivity</b>	<b>RF-Derived Surface Loss</b>	<b>RMS Surface Error</b>	<b>Ruze-Derived Surface Loss</b>	<b>Difference</b>
0.000 inch H <sub>2</sub> O	14.424 dBi	-12.329 dB	1.2036 Inch	-402.015 dB	389.686 dB
0.030 inch H <sub>2</sub> O	23.141 dBi	-3.612 dB	0.3407 Inch	-32.212 dB	28.600 dB
0.040 inch H <sub>2</sub> O	24.371 dBi	-2.382 dB	0.2620 Inch	-19.049 dB	16.667 dB
0.050 inch H <sub>2</sub> O	24.521 dBi	-2.232 dB	0.2334 Inch	-15.117 dB	12.885 dB
0.060 inch H <sub>2</sub> O	24.473 dBi	-2.280 dB	0.1885 Inch	-9.861 dB	7.580 dB
0.070 inch H <sub>2</sub> O	24.453 dBi	-2.300 dB	0.2649 Inch	-19.473 dB	17.173 dB

Several facts of note become evident from Table V. First, the pressurization with the largest directivity was at 0.050 Inch H<sub>2</sub>O with a directivity of 24.521 dBi. At this pressurization level, the surface loss experienced was -2.232 dB. The RMS surface error at this pressurization was 0.2334 inches, which correlates to a Ruze directivity

degradation of  $-15.117$  dB. This implies that the Ruze Equation overstates the directivity degradation by  $12.885$  dB.

However, the pressurization with the smallest RMS surface error was at  $0.060$  Inch  $H_2O$  with an RMS surface error of  $0.1885$  inches. This RMS surface error, according to Ruze, produces a directivity degradation of  $-9.861$  dB. The RF performance at this pressurization level was  $24.473$  dB, producing a surface loss of  $-2.280$  dB. This implies that the Ruze Equation overstates the directivity degradation by  $7.580$  dB.

For all six pressurization levels, the Ruze Equation overstates the degradation in the directivity. The lowest overstatement of the degradation in directivity was  $7.580$  dB at a pressurization of  $0.060$  Inch  $H_2O$ . The largest overstatement of the degradation in the directivity was  $389.686$  dB at a pressurization of  $0.000$  Inch  $H_2O$ , while the antenna was not inflated.

Finally, it is important to note that the Ruze Equation does not provide any information on the beam patterns that characterize the antenna. As shown in Figures 17 through 28, the first nulls off of the main beam occur at slightly different locations based on the pressurization level. Also, these nulls have different amplitudes from one another. For full characterization of the antenna performance, utilizing the Ruze Equation for the directivity degradation provides zero information on the nature of the beam patterns that define the performance of the antenna.

## **CHAPTER V**

### **CONCLUSIONS**

The Ruze Equation utilizes the RMS surface error that is calculated from photogrammetry data to compute a directivity degradation value. However, it has been shown that this surface loss that the Ruze Equation predicts is not accurate for the membrane aperture antennas of interest here. For the offset inflatable aperture antenna tested in this study, the Ruze Equation overstates the directivity degradation. At the lowest RMS surface error produced from the multiple pressurization levels that the offset inflatable aperture antenna was tested under, the Ruze Equation overstates the surface loss by 7.58 dB. However, at the worst case, when the antenna was not inflated and inverted, the Ruze Equation overstates the surface loss by about 390 dB.

It is believed that the reason why the Ruze Equation overstates the surface loss is due to the types of errors that the inflatable aperture antennas need to overcome. The Ruze Equation assumes that the errors are random in nature, are uniformly distributed over the aperture, are distributed in fixed, circular correlation regions with a diameter that is much smaller than the diameter of the antenna, and have a Gaussian spatial phase correlation. However, inflatable aperture antennas suffer from surface errors involving wrinkles due to under-inflation of the inflatable aperture antenna and the Hencky curve

near the edges of the antenna. Neither one of these errors is random on the antenna surface. Wrinkles occur along locations of the antenna where the pressurization does not create enough strain on the inflatable membrane material. Hencky type errors always occur near the edge of the antenna. Thus, Hencky type errors are not uniform over the antenna aperture. Typically, wrinkles will be present along the entire aperture if the antenna is properly inflated. Neither wrinkles nor Hencky curve errors occur in fixed, circular correlation regions. Wrinkles can take on an elliptical shape, while Hencky errors would surround the entire antenna. Therefore, the correlation regions, regardless of shape, are not much smaller than the diameter of the antenna. The dominant errors that are associated with inflatable aperture antennas do not correspond with those associated with the types of errors that Ruze Equation takes into account.

The Ruze Equation is also limited in what it can predict. While the Ruze Equation attempts to characterize the surface loss, it makes no predictions on characteristics of the secondary beam patterns. Typically, it is important to understand the locations of the first nulls off of the main beam, along with how much down below the directivity that those nulls are. Sidelobes are also not accounted for in the Ruze Equation, whether it is the peak location or the amplitude. These are important characteristics of the beam patterns of an antenna that are desired to be fully understood prior to operation of the antenna.

In conclusion of this study, a recommendation has been determined regarding the application of the Ruze Equation to estimate the surface loss for inflatable aperture antennas. The Ruze Equation overstates the surface loss experienced for inflatable aperture antennas. Testing was performed on a 0.3 meter offset inflatable aperture

antenna at 8.4 GHz at six different pressurization levels. The Ruze Equation also does not provide any information on the beam patterns of the antenna. Therefore, it is not recommended that the Ruze Equation be used to predict antenna performance for inflatable aperture antennas.

## **CHAPTER VI**

### **FUTURE WORK**

Future work of the problem that is analyzed in this study involves several areas. First, the immediate follow-on effort will be to utilize the photogrammetry data points to propagate the far-field beam patterns and directivity. The methodology will be to utilize the theory of geometrical optics and edge diffracted fields to obtain the near-field amplitude and phase plots. Fourier transform techniques will then transform the near-field data into the far-field data, from which the beam patterns and directivity can be calculated. One necessary step is to create a method to compute the direction of the reflected rays from the antenna surface. Since the antenna will not be known from a continuous function, there is not an equation that derivatives can be computed from to determine the surface normal vector. Instead, the data points surrounding the surface point in question will be utilized to determine the local tangent and normal vector to the surface point. Once the normal vector is computed, Snell's Law will be utilized to determine the vector direction that the reflected ray will travel. This software code will also be extended beyond the use for offset inflatable aperture antennas, such as for inflatable cassegrain aperture antennas.

Once the software code is functional, there are plans in place to perform dynamic photogrammetry studies of the one meter class inflatable antenna inside of a thermal vacuum chamber. Targeted or projection photogrammetry of the antenna surface will likely be performed. Alternatively, laser scanning with the use of stationary mirrors located inside the thermal vacuum chamber through windows located on the walls of the vacuum chamber may be performed.

A second proposed study is to examine the effects of gravity over time dealing with the sag on the antenna. Since the shape of the inflatable antenna is not constant over time, also caused by inflation pressurization changes, gravity can deform the shape of the inflatable antenna from the ideal paraboloid. The study would be to examine the effects of gravity over time with constant inflation pressurization to attempt to understand how the paraboloidal shape deforms over time. The goal will be to try and back out all of the effects of gravity, from before the first instance that gravity has deformed the shape, to understand how the antenna may perform in space after inflation.

The final proposed effort is to attempt to create an equation that will account for all of the types of errors associated with inflatable aperture antennas. This ideal equation would need to account for the random microscopic surface errors, such as what the Ruze Equation can handle. This equation would also need to account for the deterministic macroscopic surface errors associated with the Hencky curve, wrinkles, and over-inflation errors. This equation could provide a means of accurately approximating the directivity degradation for inflatable aperture antennas.

## REFERENCES

1. Acosta, R. and Lee, R., "Case Study of Sample Spacing in Planar Near-Field Measurement of High Gain Antennas," NASA TM-86872, Sep. 1984.
2. Balanis, C., "Antenna Theory Analysis and Design," New York, John Wiley & Sons, 1982.
3. Bao, V., "Nonconstant Correlation Interval in Antenna Tolerance Theory," IEEE Transactions on Antennas and Propagation, pp. 118-119, Jan. 1970.
4. Bao, X., Bar-Cohen, Y., Chang, Z., Sherrit, S., and Badescu, M., "Wirelessly Controllable Inflated Electroactive Polymer (EAP) Reflectors," SPIE Structures Conference, San Diego, CA, vol. 5759-52, Mar. 2005.
5. Bracewell, R., "Tolerance Theory of Large Antennas," IRE Transactions on Antennas and Propagation, pp. 49-58, 1961.
6. Cheng, D., "Effect of Arbitrary Phase Errors on the Gain and Beamwidth Characteristics of Radiation Pattern," IRE Transactions – Antennas and Propagation, pp. 145-147, 1955.
7. Cherrette, A. and Lee, S., "Detection of Reflector Surface Error from Near-Field Data: Effect of Edge Diffracted Field," NASA TM-89920, Jun. 1987.
8. Collin, R. and Zucker, F., "Antenna Theory Part 1," New York, McGraw-Hill Book Company, 1969.
9. Collin, R., "Antennas and Radiowave Propagation," New York, McGraw-Hill Book Company, 1985.
10. Colliver, C., "Extended Antenna Tolerance Theory and its Application to Satellite Antennas," University of Dayton Dissertation, Dec. 1997.
11. Freeland, R., Bilyeu, G., and Veal, G., "Validation of a Unique Concept for a Low-Cost Lightweight Space-Deployable Antenna Structure," IAF-93-I.1.204.

12. Gasper, J., Sreekantamurthy, T., Mann, T., Behun, V., Romanofsky, R., Lambert, K., and Pearson, J., "Test and Analysis of an Inflatable Parabolic Dish Antenna," 47<sup>th</sup> AIAA Structures, Structural Dynamics, and Materials Conference, May 2006.
13. Hoferer, R. and Rahmat-Samii, Y., "RF Characterization of an Inflatable Parabolic Torus Reflector Antenna for Space-Borne Applications," IEEE Transactions on Antennas and Propagation, vol. 46, no. 10, pp. 1449-1457, Oct. 1998.
14. Jenkins, C., Kalanovic, V., Padmanabhan, K., and Faisal, S., "Intelligent Shape Control for Precision Membrane Antennae and Reflectors in Space," Smart Material Structures, vol. 8, pp. 857-867, 1999.
15. Marker, D. and Jenkins, C., "Surface Precision of Optical Membranes with Curvature," Optics Express, vol. 1, no. 11, pp. 324-331, Nov. 1997.
16. Naboulsi, S., "Investigation of Geometric Imperfection in Inflatable Aerospace Structures," Journal of Aerospace Engineering, pp. 98-105, Jul. 2004.
17. Ng, T., "Edge Effects in Pressurized Membranes," Journal of Engineering Mechanics, pp. 1100-1104, Oct. 2004.
18. Pearson, J., "Phase III Inflatable Membrane Antennas," NASA TR 04-1052, Feb. 2004.
19. Pearson, J. and Romanofsky, R., "Thin Film Antenna Development and Optimization," 47<sup>th</sup> AIAA Structures, Structural Dynamics, and Materials Conference, May 2006.
20. Rahmat-Samii, Y., "An Efficient Computational Method for Characterizing the Effects of Random Surface Errors on the Average Power Pattern of Reflectors," IEEE Transactions on Antennas and Propagation, vol. AP-31, no. 1, pp. 92-98, Jan. 1983.
21. Rahmat-Samii, Y., "Useful Coordinate Transformations for Antenna Applications," IEEE Transactions on Antennas and Propagation, vol. AP-27, no. 4, pp. 571-574, Jul. 1979.

22. Romanofsky, R., Bibyk, I., Welch, B., and Lambert, K., "The Potential for Gossamer Deployable Antenna Systems in Ka-Band Exploration and Science Communications Architectures," 12<sup>th</sup> Ka-Band and Broadband Communications Conference, September 2006.
23. Ruze, J., "Antenna Tolerance Theory – A Review," Proceedings of the IEEE, vol. 54, no. 4, pp. 633-640, Apr. 1966.
24. Ruze, J., "The Effect of Aperture Errors on the Antenna Radiation Pattern," Supplemento al Nuovo Cimento, vol. 9, no. 3, pp. 364-380, 1952.
25. Thomas, M. and Friese, G., "Pressurized Antennas for Space Radars," AIAA-1980-1928, pp. 65-71.
26. Williams, W., "High Capacity Communications from Martian Distances," NASA TM-2006-214415, Mar. 2006.
27. Zarghamee, M., "A Note on the Prediction of Antenna Tolerance from Efficiency Measurements," IEEE Transactions on Antennas and Propagation, pp. 354-355, May 1969.
28. Zarghamee, M., "On Antenna Tolerance Theory," IEEE Transactions on Antennas and Propagation, vol. AP-15, no. 6, pp. 777-781, Nov. 1967.
29. Zocchi, F., "Estimation of the Accuracy of a Reflector Surface From the Measured RMS Error," IEEE Transactions on Instrumentation and Measurement, vol. 54, no. 5, pp. 2124-2129, Oct. 2005.